The role of myosin heavy chain phosphorylation in *Dictyostelium* motility, chemotaxis and F-actin localization

Paul J. Heid, Deborah Wessels, Karla J. Daniels, D. Phillip Gibson, Hui Zhang, Ed Voss and David R. Soll*

W. M. Keck Dynamic Image Analysis Facility, Department of Biological Sciences, The University of Iowa, Iowa City, IA 52242, USA
*Author for correspondence (e-mail: david-soll@uiowa.edu)

Accepted 14 June 2004
Journal of Cell Science 117, 4819-4835 Published by The Company of Biologists 2004
doi:10.1242/jcs.01358

Summary

To assess the role of myosin II heavy chain (MHC) phosphorylation in basic motility and natural chemotaxis, the *Dictyostelium mhcA* null mutant *mhcA*$^-$, *mhcA*$^-$ cells rescued with a myosin II gene that mimics the constitutively unphosphorylated state (3XALA) and *mhcA*$^-$ cells rescued with a myosin II gene that mimics the constitutively phosphorylated state (3XASP), were analyzed in buffer and in response to the individual spatial, temporal and concentration components of a cAMP wave using computer-assisted methods. Each mutant strain exhibited unique defects in cell motility and chemotaxis. Although *mhcA*$^-$ cells could crawl with some polarity and showed chemotaxis with highly reduced efficiency in a spatial gradient of cAMP, they were very slow, far less polar and more three-dimensional than control cells. They were also incapable of responding to temporal gradients of cAMP, of chemotaxis in a natural wave of cAMP or streaming late in aggregation. 3XASP cells were faster and chemotactically more efficient than *mhcA*$^-$ cells, but still incapable of responding to temporal gradients of cAMP, chemotaxis in natural waves of cAMP or streaming late in aggregation. 3XALA cells were fast, were able to respond to temporal gradients of cAMP, and responded to natural waves of cAMP. However, they exhibited a 50% reduction in chemotactic efficiency, could not stream late in aggregation and could not enter the streams of control cells in mixed cultures. F-actin staining further revealed that while the presence of unphosphorylated MHC was essential for the increase in F-actin in the cytoplasm in response to the increasing temporal gradient of cAMP in the front of a natural wave, the actual dephosphorylation event was essential for the associated increase in cortical F-actin. The results of these studies indicate that MHC phosphorylation-dephosphorylation, like myosin II regulatory light chain phosphorylation-dephosphorylation, represents a potential downstream target of the regulatory cascades emanating from the different phases of the wave.

Key words: 2D-DIAS analysis, cAMP chemotaxis, Myosin heavy chain phosphorylation, Myosin null mutant, Myosin phosphorylation mutants

Introduction

Because of its essential role in muscle contraction, it has been assumed that non-muscle myosin II plays a similar role in amoeboid cell motility. However, its actual role has not been fully ascertained, presumably because cell polarization, anterior and lateral pseudopod extension, persistent translocation, turning and chemotaxis have proved to be far more complex behavioral phenomena than originally assumed (Soll et al., 2003). More surprising, null mutants of myosin II, first generated in *Dictyostelium discoideum* (DeLozanne and Spudich, 1987; Knecht and Loomis, 1987), proved not only to be viable, but also capable of pseudopod extension, cellular translocation and even chemotaxis, although in all cases the behaviors were aberrant (Wessels et al., 1988; Peters et al., 1988).

Dictyostelium provides a unique experimental system for exploring the role of myosin II in cell motility and chemotaxis (Spudich, 1989), not only because it is readily amenable to mutational studies because of its haploid nature (Kessin, 2001; Kuspa and Loomis, 1994), but also because both motility and chemotaxis of normal *Dictyostelium* amoebae have been subjected to exhaustive computer-assisted analysis in order to facilitate the characterization of mutant behavior (Soll et al., 2003). *Dicytostelium* possesses a single myosin II, composed of two heavy chains, two essential light chains and two regulatory light chains (Spudich, 1989; Yumura and Uyeda, 2003). It appears to be distributed at low levels throughout the cytoplasm and localized in the cell cortex, but excluded from pseudopods (Fukui, 1990; Fukui *et al*., 1987), except during retraction (Moores et al., 1996). When suspension cultures of *Dictyostelium* amoebae are treated with cAMP, both the myosin II heavy chain and regulatory light chain are transiently phosphorylated (Kuczmarski and Spudich, 1980; Berlot et al., 1985; Berlot et al., 1987), indicating that phosphorylation, which regulates myosin polymerization (Kuczmarski and Spudich, 1980; Côté and McCrea, 1987; Ravid and Spudich, 1989), may be involved in chemotaxis. Phosphorylation mutants of myosin heavy chain have revealed that phosphorylation-dephosphorylation plays a role in cell behavior. The mutant 3XALA, which possesses a myosin II heavy chain that mimics the constitutively unphosphorylated state (i.e. it cannot be phosphorylated) (Egelhoff et al., 1993),

overassembles myosin II in the cortex, exhibits increased cortical tension (Egelhoff et al., 1993; Egelhoff et al., 1996; Luck-Vielmetter et al., 1990), undergoes abnormal pseudopod bifurcation and exhibits a decrease in chemotactic efficiency in a spatial gradient of attractant (Stites et al., 1998). The mutant S13A, which possesses a myosin regulatory light chain that mimics the constitutively dephosphorylated state (i.e. it cannot be phosphorylated) (Ostrow et al., 1994), exhibits a defect in basic motile behavior, specifically a decrease in lateral pseudopod formation, an actual increase in chemotactic efficiency, and a major defect in its response to the decreasing temporal gradient in the back of a natural wave (Zhang et al., 2002).

Although the regulatory light chain phosphorylation mutant S13A has been subjected to the full set of experimental protocols developed to analyze basic motile behavior in the absence of chemoattractant and the behavioral responses to the individual spatial, temporal and concentration components of the natural cAMP wave (Zhang et al., 2002), neither the myosin null mutant *mhcA*$^-$, nor the phosphorylation mutants 3XALA and 3XASP, have been analyzed in a similar fashion. It has, therefore, not been possible to integrate the phosphorylation-dephosphorylation of MHC into models of the molecular cascades emanating from the different phases of the natural wave that regulate chemotactic behavior, as has been done for the phosphorylation-dephosphorylation of the myosin II regulatory light chain (Wessels et al., 2004). To this end, we have subjected the *mhcA*$^-$, 3XALA and 3XASP mutants to two-dimensional (2D) and three-dimensional (3D) computer-assisted reconstruction and motion analysis in the following conditions: (1) in the absence of chemoattractant (basic motile behavior), (2) in a spatial gradient of chemoattractant, which orients cells at the onset of the front of a natural wave, (3) in increasing temporal gradients of attractant, which regulate behavior in the front of natural waves, (4) in decreasing temporal gradients of attractant, which regulate behavior in the back of natural waves, (5) in response to natural waves of cAMP relayed by a majority of control cells in mixed aggregation cultures and (6) during streaming, the last stage in natural aggregation (Soll et al., 2003). Our results indicate that myosin II heavy chain phosphorylation-dephosphorylation, like myosin II regulatory light chain phosphorylation-dephosphorylation, plays a fundamental role in the basic motile behavior of a cell, and represents a potential downstream target of the regulatory cascades emanating from the different phases of the natural wave. Furthermore, our results indicate that while the presence of unphosphorylated MHC is essential for the increase in F-actin in the cytoplasm in response to the increasing temporal gradient of cAMP in the front of the wave, the actual process of MHC dephosphorylation is essential for the associated increase in F-actin localization in the cell cortex.

Materials and Methods

Origin and maintenance of strains

The parental JH10 strain, the *mhcA* null mutant strain, referred to here as *mhcA*$^-$, the myosin heavy chain phosphorylation mutants 3XALA and 3XASP and the *mhcA*$^-$ strain rescued with wild-type *mhcA*, referred to here as *mhcA*$^-$/*mhcA*$^+$, have been described previously (Manstein et al., 1989; Egelhoff et al., 1993). Briefly, the mutant *mhcA*$^-$ was constructed from the *mhcA*$^+$*thy*$^-$ cell line JH10 by targeted gene replacement via homologous recombination of *mhcA* with an *mhcA* construct disrupted with the *thy1* marker (Manstein et al., 1989). The *mhcA*$^-$/*mhcA*$^+$ rescued strain was generated by transforming *mhcA*$^-$ cells with an autonomously replicating vector containing a G418-resistant gene cassette and the wild-type *mhcA* coding region regulated by the actin 15 promoter (Egelhoff et al., 1993). 3XALA mutant cells were generated in a manner similar to *mhcA*$^-$/*mhcA*$^+$, but in this case threonines in the *mhcA* coding region at positions 1823, 1833 and 2029, were mutated to alanine residues (Egelhoff et al., 1993). 3XASP mutant cells were generated in a manner similar to 3XALA cells, except that the same threonine residues were mutated to aspartate residues (Egelhoff et al., 1993). Cells of all strains were grown in submerged plate cultures since attachment promoted a higher proportion of mononuclear cells amongst the *mhcA*$^-$ and 3XASP cell lines. For experimental purposes, cells were harvested from plates at the confluent monolayer stage, washed with buffered salts solution (BSS: 20 mM KCl, 2.5 mM $MgCl_2$, 20 mM KH_2PO_4, pH 6.4) and distributed on filter pads saturated with BSS at a cell density of 5×10^6 per cm^2. For all five cell lines, cells were washed from filter pads at the ripple stage, which represents the onset of aggregation (Soll, 1979) and the time at which wild-type cells achieve maximum velocity (Varnum et al., 1986).

Basic motile behavior

Cells were washed from filter pads and distributed on the glass wall of a Sykes-Moore perfusion chamber (Bellco Glass, Vineland, NJ, USA) positioned on the stage of an upright microscope with long distance working condenser and a bright field 25× magnification objective, as previously described (Falk et al., 2003; Zhang et al., 2003). After 5 minutes of incubation, the chamber was perfused with BSS at a rate that turned over one chamber volume-equivalent every 15 seconds. Cells were continuously videorecorded for 10 minutes.

Spatial gradient of cAMP

Cells were dispersed either on the bridge of a Plexiglas chemotaxis chamber (Varnum and Soll, 1984) designed after that of Zigmond (Zigmond, 1977) for bright-field analysis, or on the bridge of a quartz chamber for differential interference contrast (DIC) microscopy (Shutt et al., 1998). BSS alone was added to one of the two wells bordering the bridge and to the other, BSS containing 10^{-6} M cAMP. Cells were incubated for 5 minutes to facilitate cell adhesion and allow for the genesis of a steep gradient of chemoattractant across the bridge, then videorecorded for 10 minutes.

Simulated temporal waves of cAMP

Cells were treated with a series of four temporal waves of cAMP generated in the absence of established spatial gradients in a Sykes-Moore perfusion chamber, using NE-1000 Multi-Phaser Programmable Syringe Pumps (New Era Pump Systems, Wantagh, NY, USA) as previously described (Geiger et al., 2003). Cells were videorecorded through the four waves, representing a time period of 28 minutes.

Natural cAMP waves and streaming

Mutant cells were labeled with DiI (Molecular Probes, Eugene, OR), mixed with unlabeled control cells at a ratio of 1 labelled:9 unlabelled, and plated in submerged cultures according to the method of Wessels et al. (Wessels et al., 2004). Cultures were analyzed with a BioRad Radiance 2100MP laser scanning confocal microscope (LSCM) (BioRad, Hemel Hempstead, UK). Transmitted and fluorescent images were simultaneously collected every 20 seconds and averaged using LaserSharp 2000 software (BioRad). These movies were then converted to QuickTime format.

To examine streaming during the late phases of aggregation, growth phase cells at the monolayer stage were scraped from the surface of Petri plates, pelleted and washed three times in BSS. Cells at a density of 3.5×10^7 cells/ml in a volume of 400 μl were then spread evenly on 10 cm dishes coated with 2% agar in BBS. The plates were incubated at 22°C in a humidity chamber and photographed at the onset of streaming at 18× magnification using a Nikon CoolPix camera mounted on a dissection microscope.

Two dimensional computer-assisted analysis

Video images were digitized onto the hard drive of a Macintosh computer at a rate of 15 frames per minute (4 second intervals) with a frame-grabber board (Data Translation Inc., Marlboro, MA, USA). 2D-DIAS software then was used for computer-assisted two-dimensional analyses as previously described (Soll, 1995; Soll and Voss, 1998). However, in contrast to earlier studies (e.g. Zhang et al., 2002; Zhang et al., 2003; Wessels et al., 2004) no velocity threshold was used for selecting cells for analysis (i.e. all cells were analyzed). Cell perimeters were automatically outlined using the grayscale threshold algorithm. Outlines were converted to beta-spline replacement images. Motility parameters were computed from the centroid positions and dynamic morphology parameters from contours of the replacement images. Instantaneous velocity, directional change, maximum length and roundness were computed as previously described (Soll, 1995; Soll and Voss, 1998; Wessels et al., 2004). Persistence was computed as the net distance between the first and last centroid for the entire period of analysis (~5 to 10 minutes) divided by the summed distance between centroids that were generated every 4 seconds (Wessels et al., 2004). 'Chemotactic index' (CI) was computed as the net distance traveled directly towards the source of chemoattractant in a spatial gradient chamber, divided by the summed distance between centroids generated every 4 seconds. 'Percent positive chemotaxis' was the proportion of cells exhibiting a positive CI in a spatial gradient of cAMP over the period of analysis. Difference pictures were generated by superimposing frame *n*-1 over frame *n*.

'Expansion zones' were demarcated in green as regions in the cell outline in frame *n* not overlapping the cell outline in frame *n*-1. 'Contraction zones' were demarcated in red as regions in the cell outline in frame *n*-1 not overlapping the cell outline in frame *n*. All stacking and difference pictures along with the new vector tracking feature were drawn at 300 dpi resolution using the new JAVA-based DIAS 4.0 system (E.V. and D.R.S., in preparation).

Three dimensional computer-assisted reconstruction

Cells were optically sectioned and reconstructed using 3D-DIAS software as previously described (Zhang et al., 2003; Wessels et al., 1998; Wessels et al., 2004). In brief, 60 optical sections were collected in a 2-second period at 0.3 μm increments using DIC optics. This process was repeated every 5 seconds. The image was converted to a digital image and captured directly onto the computer hard drive using iMovie software. The resulting iMovie was compressed into the DIAS format. 3D-DIAS software in the newly developed JAVA-based DIAS 4.0 platform (E.V. and D.R.S., in preparation) automatically outlined the perimeter of the in-focus portion of the image in each optical section using a pixel complexity algorithm (Soll et al., 1998). The distal nonparticulate zones of pseudopodial regions were manually outlined in the in-focus portions of each optical section to generate a faceted 3D reconstruction of pseudopods, which were color-coded yellow and inserted into the nontransparent faceted cell image, which was color-coded blue.

Western analysis of myosin II

For western analysis of MHC, 2×10^7 washed cells were suspended in 1 ml of lysis buffer containing 75 mM β-glycerophosphate, 20 mM Mops, pH 7.2, 15 mM EGTA, 2 mM EDTA, 1 mM sodium orthovanadate, 1 mM DTT, 20 μg/ml leupeptin, 20 μg/ml antipain and 20 μg/ml aprotinin (Khosla et al., 2000). Protein concentrations were determined by the method of Bradford (Bradford, 1976). An aliquot containing 20 μg of protein was mixed 1:2 with SDS rescuing buffer (5% β-mercaptoethanol, 0.5% SDS, 6.25 mM Tris-HCl, pH 6.8, 12.5% glycerol, 0.04% Bromophenol Blue), incubated at 95°C for 4 minutes and subjected to SDS-polyacrylamide gel electrophoresis (Laemmli, 1970). The proteins were then transferred to a PVDF membrane (Immobilon-P, Millipore Corporation, Bedford, MA, USA) using a Trans-Blot semi-dry electrophoretic transfer cell (Bio-Rad, Hercules, CA, USA) and a single buffer system (Bjerrum and Schafer-Nielsen, 1986). The membranes were blocked overnight in blocking solution (Zymed Laboratories, San Francisco, CA, USA). Rabbit anti-myosin II antibody, a generous gift from Arturo DeLozanne (University of Texas, Austin, USA), was diluted 1:1000 and incubated with the membranes for 2 hours at room temperature. The membrane was then washed four times in Tris-buffered saline (TBS)-T (25 mM Tris-HCl, pH 7.4, 0.15 M NaCl, 0.05% Tween 20). The primary antibody was detected using HRP-labeled goat anti-rabbit IgG (Promega, Madison, WI), diluted 1:20,000 in blocking solution, developed with Super Signal West Pico Thermoluminescent Substrate (Pierce, Rockford, IL, USA) and exposed to X-ray film (Eastman Kodak, Rochester, NY, USA).

Fluorescent staining

For both nuclear and F-actin staining, cells were fixed with 4% paraformaldehyde in 10 mM Mes [2(N-morpholino) ethanesulfonic acid; Sigma, St Louis, MO, USA) buffer (pH 6.1) containing 138 mM KCl, 3 mM $MgCl_2$ and 2 mM EGTA. Nuclear staining was performed as described previously (Lockhart et al., 2003) with Hoechst 33342 (Molecular Probes, Eugene, OR, USA). Stained cells were mounted in Moviol. For F-actin localization, cells were stained with Oregon Green®-phalloidin (Molecular Probes, Inc., Eugene, OR, USA) according to methods previously described (Zhang et al., 2002; Zhang et al., 2003). Stained cells were then imaged using the BioRad Radiance 2100MP laser scanning confocal microscope (LSCM) at 0.2 μm z-axis increments and the z-series projected as a single image ('projection image'). To obtain comparable measures of the intensity of F-actin staining in the cortex and cytoplasm, an optical section of an *mhcA*$^-$/*mhcA*$^+$ cell 1 μm above the substratum was scanned and the image optimized. The optimized LSCM parameters for this reference cell (laser power, iris aperture, gain and scan rate) were then used to obtain scans 1 μm above the substratum for mutant cell types. Line profiles of grayscale intensity were obtained just posterior to the cell nucleus through the cytoplasm and cortex in a region devoid of pseudopod extensions using BioRad LaserSharp2000 software (BioRad). Line graphs of grayscale values were generated using Microsoft Excel®. Digital images of XY planes, line profiles and projected Z-series image stacks were processed using Adobe Photoshop® software.

Results

Cytokinesis and development

The ripple stage of development, which represents the onset of aggregation (Soll, 1979), occurred in filter pad cultures of JH10, *mhcA*$^-$/*mhcA*$^+$ and 3XALA cells after 6 hours, and in *mhcA*$^-$ and 3XASP cells after 9.0 hours. For purposes of comparison, cells of all tested strains were harvested at the ripple stage, since *Dictyostelium* amoebae attain maximum single cell velocity at this stage (Varnum et al., 1986).

It had previously been reported that *mhcA*$^-$ and 3XASP cells

(DeLozanne and Spudich, 1987; Knecht and Loomis, 1987; Egelhoff et al., 1993) exhibited growth abnormalities. To assess the proportion of mononuclear cells in each test population at the time of analysis, cells were stained with Hoechst 33342. While the proportions of multinuclear cells in strains JH10, *mhcA*$^{-}$/*mhcA*$^{+}$ and 3XALA cells were 13%, 17% and 6%, respectively, the proportions in strains *mhcA*$^{-}$ and 3XASP were 53% and 62%, respectively. For all analyzed strains, only mononuclear cells, assessed by visualizing nuclei through either differential interference contrast or phase-contrast microscopy, were analyzed in behavioral studies.

The proper controls for mutant cell lines

For the null mutant *mhcA*$^{-}$, the parental strain JH10 served as a proper control (Manstein et al., 1989). However, mutants 3XALA and 3XASP were generated by rescuing the null mutant *mhcA*$^{-}$ with mutated forms of the *mhcA* open reading frame under the regulation of the actin 15 promoter in a nonintegrating plasmid (Egelhoff et al., 1993). Because the actin 15 promoter is very likely stronger than the native *mhcA* promoter, strain *mhcA*$^{-}$/*mhcA*$^{+}$ represented a more appropriate control than JH10, since it was generated by rescuing the same *mhcA*$^{-}$ strain with the wild-type *mhcA* open reading frame under the same actin promoter in the same nonintegrating plasmid (Egelhoff et al., 1993). This decision to use this strain was based on a comparison of the motile behavior of JH10 and *mhcA*$^{-}$/*mhcA*$^{+}$ cells in buffer. While they migrated in buffer in a fashion similar to that of JH10 cells, *mhcA*$^{-}$/*mhcA*$^{+}$ cells translocated at slightly reduced velocity with slightly less persistence (see Table 1). These differences were apparent in perimeter tracks. Those of JH10 cells (Fig. 1A) were on average slightly longer and slightly more persistent than those of *mhcA*$^{-}$/*mhcA*$^{+}$ cells (Fig. 1C).

The slight but consistent differences in the basic motile behavior of JH10 and *mhcA*$^{-}$/*mhcA*$^{+}$ cells could be due to differences in the levels of MHC resulting from differences in the strength of the promoters regulating *mhcA* expression in the two strains, the endogenous promoter in the case of JH10 versus the actin 15 promoter in the case of *mhcA*$^{-}$/*mhcA*$^{+}$. To test this directly, we compared the level of MHC protein in each strain by probing western blots with anti-MHC antibody. One band was identified for parental JH10 cells, while no signal was observed for *mhcA*$^{-}$ cells (Fig. 2). One band of the same molecular mass was also identified in *mhcA*$^{-}$/*mhcA*$^{+}$, 3XALA and 3XASP cells, but the intensity of the MHC band from the three latter strains was approximately twice that from JH10 cells (Fig. 2). These reproducible results reinforced the decision to use *mhcA*$^{-}$/*mhcA*$^{+}$ as the relevant control for 3XALA and 3XASP cells.

The basic motile behavior of *mhcA*$^{-}$ cells

In the first computer-assisted analysis of *mhcA*$^{-}$ cell behavior using the original 2D motion analysis system DMS (Soll, 1988; Soll et al., 1988), it was concluded that *mhcA*$^{-}$ cells actively formed small pseudopods, but did not translocate in a persistent fashion, and, therefore, appeared apolar. Here, using the higher resolution motion analysis system DIAS (Soll, 1995; Soll and Voss, 1998) similar results were obtained. While the mean instantaneous velocity of JH10 cells in buffer was 10.3±4.9 μm per minute, that of *mhcA*$^{-}$ cells was 3.6±1.6 μm per minute (Table 1). The mean directional change parameter of *mhcA*$^{-}$ cells was approximately twice that of JH10 cells and the mean persistence parameter approximately eight-fold lower than that of JH10 cells (Table 1), demonstrating that in addition to a dramatic reduction in velocity, there was also a dramatic reduction in the directional persistence of cellular translocation. *mhcA*$^{-}$ cells were also rounder than JH10 cells, as evidenced by a significantly lower mean maximum length and a significantly higher mean roundness value (Table 1). The differences in velocity and cell shape were evident in perimeter tracks (Fig. 1B).

Although the average 2D-DIAS data (Table 1) suggested that *mhcA*$^{-}$ cells made little net progress in a particular direction and were far less polar than JH10 cells, scrutiny of perimeter tracks

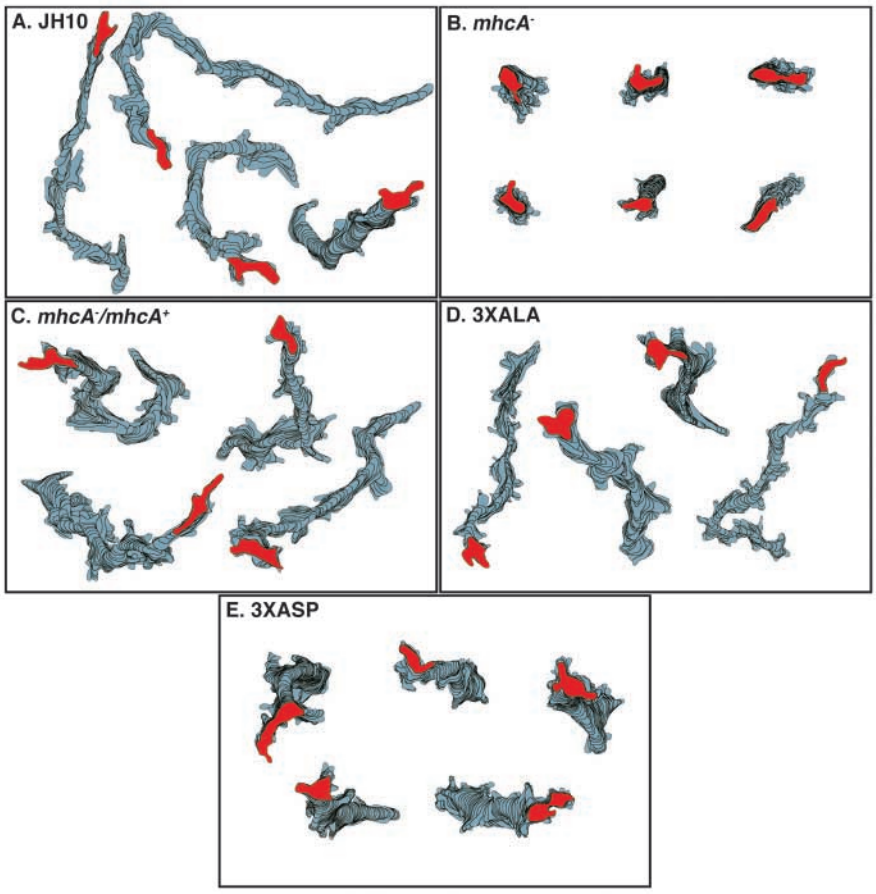

Fig. 1. Perimeter tracks of representative control and mutant cells translocating in buffer, in the absence of chemoattractant. For each cell type, cells were selected that portrayed the range of behavior. The red cell image represents the last one in each track. Cells were reconstructed at 8-second intervals. Notice that while JH10 is the control for *mhcA*$^{-}$, *mhcA*$^{-}$/ *mhcA*$^{+}$ is the control for 3XALA and 3XASP.

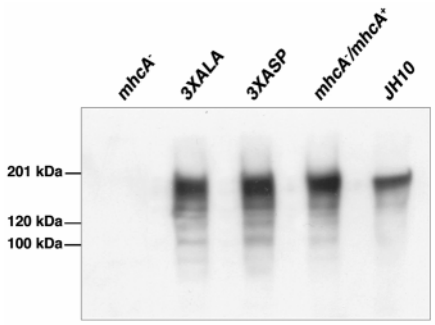

Fig. 2. Western blot analysis of MHC levels in JH10, *mhcA*$^{-}$, *mhcA*$^{-}$/*mhcA*$^{+}$, 3XALA and 3XASP. Notice that the levels in *mhcA*$^{-}$/*mhcA*$^{+}$, 3XALA and 3XASP are equivalent, and at least twice that in JH10.

(Fig. 1B) suggested that there was more to the story. Of the six randomly selected perimeter tracks of *mhcA*$^{-}$ cells in Fig. 1B, three appeared persistent, although still highly contracted when compared to those of JH10 cells. An analysis of the average motility parameters of each of these persistent cells revealed that they were among the fastest of the 47 *mhcA*$^{-}$ cells individually analyzed in buffer. We therefore selectively computed the motility and morphology parameters for the ten fastest *mhcA*$^{-}$ cells (Table 1). The mean instantaneous velocity of this subset was 6.1±0.7 μm per minute, roughly twice the mean for the entire *mhcA*$^{-}$ cell population, but still significantly lower than that of JH10 cells (Table 1). The mean maximum length and mean roundness parameter of the 10 fastest *mhcA*$^{-}$ cells were more similar to those of JH10 cells than to the entire *mhcA*$^{-}$ cell population (Table 1). However, the mean directional change and persistence parameters were still abnormally high and low, respectively, as they were for the entire population of *mhcA*$^{-}$ cells (Table 1). Therefore, although the overall perimeter tracks of the fastest *mhcA*$^{-}$ cells revealed directional persistence, quantitative measures based upon the cell centroid still suggested a high level of directional instability.

To explore this point further, tracks of translocation vectors were generated from the centroid tracks of JH10 cells and the fastest *mhcA*$^{-}$ cells. A vector represented the direction of net translocation for the period between sequential centroids, computed at 8-second intervals in this case. The vectors of persistently translocating JH10 cells were pointing relatively uniformly in the direction of persistent translocation (Fig. 3A). In difference pictures generated at 8-second intervals for the same JH10 cell (Fig. 3A), a single compact expansion zone (green) localized to the very anterior end of the elongate cell body. The tracks of vectors computed in a similar fashion for the fastest *mhcA*$^{-}$ cells were directionally far less constant than those of JH10 cells, even though the perimeter track demonstrated net translocation in a single direction (Fig. 3B). In the corresponding difference pictures of the representative *mhcA*$^{-}$ cell, expansion zones did not localize to the anterior end of the cell (Fig. 3B), as they did in difference pictures of JH10 cells (Fig. 3A). Rather, they were less compact and on average rimmed the anterior half of the cell perimeter. A similar 2D analysis of nine additional JH10 and nine additional *mhcA*$^{-}$ cells provided similar results.

One possible explanation for the directional instability of *mhcA*$^{-}$ cells was that they underwent abnormal z-axis expansion, undetectable in 2D analyses. This was suggested in side view images of live *mhcA*$^{-}$ cells obtained by Sheldon and Knecht (Sheldon and Knecht, 1996). *mhcA*$^{-}$ and control cells translocating in buffer were, therefore, reconstructed in 3D at short time intervals using 3D-DIAS software (Soll and Voss, 1998; Soll et al., 2000; Wessels et al., 1998). In each reconstruction, pseudopodia were color-coded yellow and the cell body was light blue. The representative JH10 cell in Fig. 4A exhibited anterior-posterior elongation along the substratum and a dominant, compact anterior pseudopod extended in the direction of cellular translocation. Between 0 and 16 seconds, this cell retracted a lateral pseudopod that it had extended above the substratum prior to the sequence shown (Fig. 4A). 3D reconstructions of four additional JH10 cells revealed a similar elongate shape along the substratum, a dominant compact anterior pseudopod, and coordinated extension and retraction of lateral pseudopods (data not shown). In marked contrast, 3D reconstructions of *mhcA*$^{-}$ cells of average speed revealed a mound-shaped cell body and a dominant pseudopod frequently positioned atop the cell body (Fig. 4B), which explains why a compact anterior pseudopod was not continually evident in 2D *mhcA*$^{-}$ difference pictures (Fig. 3B). Minor pseudopods continually formed from the perimeter of the representative *mhcA*$^{-}$ cell

Table 1. 2D-DIAS analysis of cell behavior in buffer, in the absence of cAMP.

Cell type	No. of cells	Instantaneous velocity (μm/minute)	Directional change (deg/4 second)	Persistence (net/total dist.)	Maximum length (μm)	Roundness (%)
JH10	50	10.3±4.9	33.8±13.4	0.41±0.20	20.0±3.5	53.4±12.0
mhcA^{-}	47	3.6±1.6	64.4±7.4	0.05±0.04	14.8±4.5	75.1±15.0
mhcA^{-} (fastest)	10	6.1±0.7	60.8±6.6	0.05±0.01	19.3±4.3	59.2±13.0
mhcA^{-}/*mhcA*$^{+}$	49	7.3±2.4	47.1±9.8	0.28±0.14	18.2±3.4	57.4±12.2
3XALA	85	7.4±3.8	46.1±13.3	0.31±0.21	16.6±3.2	65.2±14.5
3XASP	41	5.5±2.1	49.0±10.2	0.25±0.16	18.3±3.0	59.8±12.8
P values						
JH10 vs *mhcA*$^{-}$		3.4×10^{-13}	5.1×10^{-23}	2.8×10^{-17}	9.2×10^{-9}	8.7×10^{-12}
JH10 vs *mhcA*$^{-}$/*mhcA*$^{+}$		2.7×10^{-4}	1.6×10^{-7}	3.3×10^{-4}	1.4×10^{-2}	NS
mhcA^{-}/*mhcA*$^{+}$ vs 3XALA		NS	NS	NS	2.1×10^{-2}	3.1×10^{-3}
mhcA^{-}/*mhcA*$^{+}$ vs 3XASP		2.4×10^{-4}	NS	NS	NS	NS
mhcA^{-} vs 3XASP		3.8×10^{-6}	1.7×10^{-11}	2.1×10^{-9}	3.8×10^{-4}	1.7×10^{-6}

Values in the top half of the table are means±standard deviation.

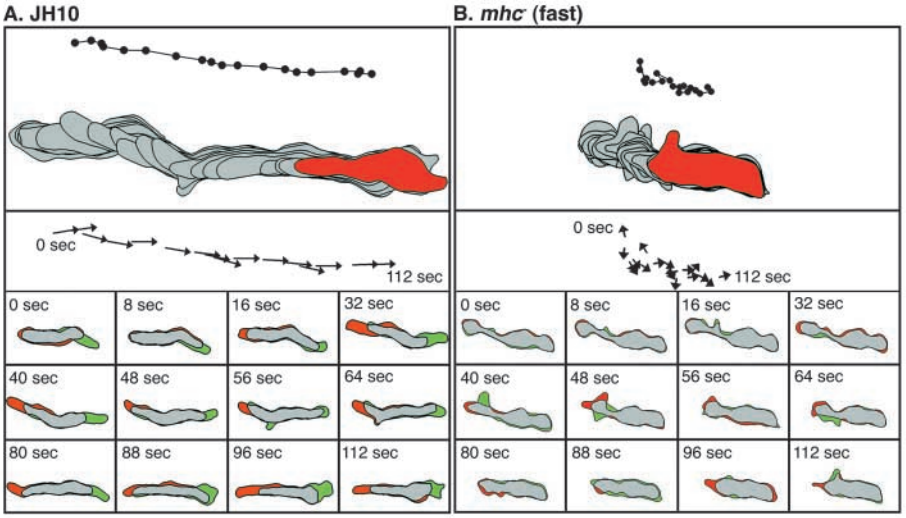

Fig. 3. A comparison of translocation between a representative JH10 (A) and a representative *mhcA*⁻ cell (B) in buffer. Top panels: centroid and perimeter plots of representative JH10 and fast *mhcA*⁻ cells. The red image is the last in the track. Middle panels: vector plots of representative JH10 and *mhcA*⁻ cells. Bottom panels: difference pictures of representative JH10 and *mhcA*⁻ cell. Vectors were computed between centroids at 8-second intervals. Green and red zones represent expansion and contraction zones, respectively.

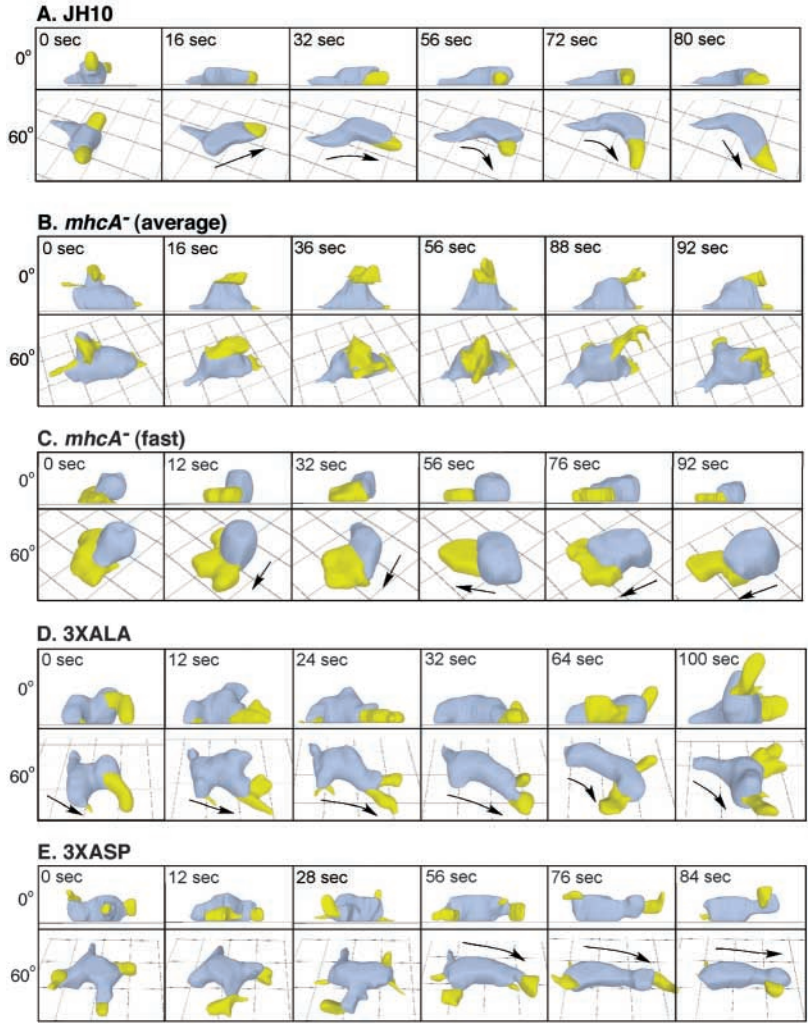

Fig. 4. 3D-DIAS reconstruction of a representative JH10 cell (A), *mhcA*⁻ cell (B), fast *mhcA*⁻ cell (C), 3XALA cell (D) and 3XASP cell (E) in buffer. Cell bodies are color-coded pale blue and pseudopods yellow. Each cell was viewed at 0 degrees (0°) and 60 degrees (60°). Arrows in A, C, D and E indicate direction of translocation.

(Fig. 4B). The dominant as well as minor pseudopods formed by *mhcA*⁻ cells had more complex, dynamic contours (Fig. 4B) than the dominant pseudopod of JH10 cells (Fig. 4A). Major and minor pseudopods frequently fragmented or coalesced. 3D reconstructions of four additional *mhcA*⁻ cells of average speed revealed similar abnormalities. 3D reconstruction of the fastest *mhcA*⁻ cells again revealed a rounder cell body, but in contrast to average *mhcA*⁻ cells (Fig. 4B), they possessed a single anterior pseudopod that extended along the substratum (Fig. 4C). This pseudopod was far broader than that of JH10 cells, resembling a thick lamellipod extending from the anterior one-third of the cell body (Fig. 4C). The contour of the broad pseudopod of fast *mhcA*⁻ cells was again more complex than that of JH10 cells, changing continuously. 3D reconstructions of four additional fast *mhcA*⁻ cells revealed the same broad, dynamic pseudopod on the substratum, and rounder cell shape.

The basic motile behavior of 3XALA cells

3XALA cells behaved in many respects like control strain *mhcA*⁻/*mhcA*⁺ cells in buffer. Mean instantaneous velocity, directional change and persistence were statistically indistinguishable (Table 1). Perimeter tracks of representative cells were consistent with these results. The tracks of *mhcA*⁻/*mhcA*⁺ cells (Fig. 1C) and 3XALA cells (Fig. 1D) were of similar length and exhibited comparable frequencies of sharp turns. Vector tracks of 3XALA and *mhcA*⁻/ *mhcA*⁺ cells in buffer were both persistent (data not shown), like JH10 cells (Fig. 3A). However, the shape parameters of 3XALA and *mhcA*⁻/*mhcA*⁺ cells differed. The mean maximum length of 3XALA cells was significantly less and the mean roundness parameter significantly greater than that of *mhcA*⁻/*mhcA*⁺ cells (Table 1).

3D reconstruction of live *mhcA*$^{-}$/*mhcA*$^{+}$ cells translocating in buffer revealed an elongate shape, a single dominant compact anterior pseudopod and intermittent lateral pseudopod formation (data not shown), similar to that of JH10 cells (Fig. 4A). 3D reconstruction of live 3XALA cells translocating in buffer also revealed an elongate cell shape and a single dominant anterior pseudopod (Fig. 4D). However, 3XALA cells were on average less elongate than *mhcA*$^{-}$/*mhcA*$^{+}$ cells, and frequently underwent pseudopod bifurcation, as exemplified in the sequence of reconstructions (Fig. 4D). A similar 3D analysis of four additional *mhcA*$^{-}$/*mhcA*$^{+}$ cells and four additional 3XALA cells supported these conclusions.

The basic motile behavior of 3XASP

The mean instantaneous velocity of 3XASP cells was significantly lower than that of *mhcA*$^{-}$/*mhcA*$^{+}$ cells, but significantly higher than that of *mhcA*$^{-}$ cells (Table 1). However, mean directional change and mean persistence were similar to those of control *mhcA*$^{-}$/*mhcA*$^{+}$ cells (Table 1). Perimeter tracks of representative 3XASP cells were consistent with these results. Although the tracks (Fig. 1E) were more compact than those of *mhcA*$^{-}$/*mhcA*$^{+}$ cells (Fig. 1C), they appeared directional and persistent.

Although the 2D-DIAS analysis of 3XASP cells translocating in buffer revealed no significant abnormalities in shape, 3D reconstructions revealed unusual pseudopod dynamics. 3XASP cells commonly manifested anterior-posterior elongation in the x,y-axes, and frequently extended a dominant anterior pseudopod on the substratum in the direction of translocation (56-76 seconds; Fig. 4E), in a general way like control cells. However, 3XASP cells frequently extended multiple lateral pseudopods from random positions around the main cell body (0-28 seconds; Fig. 4E). In some cases, pseudopods became quite long. These complex two-dimensional changes in cell contour explain the low average roundness parameter. These results suggest that the behavioral phenotype of 3XASP is distinct from *mhcA*$^{-}$ cells and, in many respects, far less severe.

mhcA^{-} cells show chemotaxis in spatial gradients of cAMP

It was previously demonstrated that while *mhcA*$^{-}$ cells could respond biochemically to the chemoattractant cAMP (Peters et al., 1988), single cell chemotaxis in a spatial gradient of cAMP was severely impaired (Wessels et al., 1988). Here, we have re-examined this process. In a spatial gradient of cAMP, *mhcA*$^{-}$ cells exhibited a slightly higher mean instantaneous velocity, a slightly lower mean directional change parameter and a dramatically higher persistence value than they did in buffer (compare Table 1 and Table 2). However, the mean instantaneous velocity of *mhcA*$^{-}$ cells in a gradient was still far lower, the mean directional change far higher, and the mean persistence parameter far lower than that of JH10 cells in a gradient (Table 2). Perimeter tracks of *mhcA*$^{-}$ cells, although shorter than those of JH10 cells, revealed a level of directional persistence (Fig. 5B) greater than that in buffer (Fig. 1B), consistent with the higher mean persistence parameter (Table 2). These results indicated that *mhcA*$^{-}$ cells responded to chemoattractant. However, the average track of *mhcA*$^{-}$ cells appeared to be random in relation to the direction of the spatial gradient of cAMP (Fig. 5B), which is reflected in the computed mean chemotactic index of *mhcA*$^{-}$ cells, which was +0.05±0.21 compared to +0.48±0.32 for JH10 cells (Table 2). These results suggested that although chemokinetically stimulated, *mhcA*$^{-}$ cells were not chemotactically stimulated. However, the percentage of *mhcA*$^{-}$ cells with a positive chemotactic index was 66%, just high enough to suggest a very weak chemotactic response (Table 2).

Based upon the observation that the fastest *mhcA*$^{-}$ cells exhibited more directional persistence in buffer (Table 1), and earlier observations that the fastest *mhcA*$^{-}$ cells showed chemotaxis in a spatial gradient of cAMP (Wessels et al., 1988), the behavior of the ten fastest *mhcA*$^{-}$ cells was selectively analyzed in a spatial gradient of cAMP. The mean instantaneous velocity of the fastest *mhcA*$^{-}$ cells was 6.6±1.4 μm per minute, close to 50% faster than the mean for all *mhcA*$^{-}$ cells, but still significantly lower than that of JH10 cells in a spatial gradient of cAMP (Table 2). The mean directional change parameter of the ten fastest *mhcA*$^{-}$ cells was lower and the mean persistence measure higher than that of the entire *mhcA*$^{-}$ population, but in both cases still different from that of JH10 cells (Table 2). The mean roundness parameter and the mean maximum length parameter of the ten fastest *mhcA*$^{-}$ cells, however, approached that of JH10 cells (Table 2). More importantly, the average chemotactic index of the ten fastest *mhcA*$^{-}$ cells was +0.12±0.32 μm per minute, far higher than

Table 2. 2D-DIAS analysis of chemotaxis in a spatial gradient of cAMP

Cell type	No. of cells	Instantaneous velocity (μm/minute)	Directional change (deg/4 seconds)	Persistence (net/total dist.)	Maximum length (μm)	Roundness (%)	Chemotactic index	Percent positive chemotaxis
JH10	39	9.1±3.6	27.1±0.3	0.65±0.19	18.6±3.8	55.1±10.9	+0.48±0.32	90%
mhcA^{-}	35	4.2±1.8	55.5±14.9	0.26±0.16	16.0±5.2	72.7±14.2	+0.05±0.21	66%
mhcA^{-} (fastest)	10	6.6±1.4	48.5±15.2	0.37±0.18	21.3±6.5	56.5±10.1	+0.12±0.32	80%
mhcA^{-}/*mhcA*$^{+}$	52	9.2±4.0	26.7±11.9	0.67±0.19	18.4±3.7	62.2±9.0	+0.48±0.37	85%
3XALA	47	8.9±4.2	26.9±13.3	0.62±0.20	18.3±3.1	61.4±8.8	+0.22±0.48	74%
3XASP	48	5.2±1.2	49.0±9.5	0.43±0.15	14.3±3.4	54.7±13.1	+0.40±0.15	98%
P values								
JH10 vs *mhcA*$^{-}$		2.4×10^{-10}	2.0×10^{-13}	2.7×10^{-14}	1.7×10^{-2}	1.4×10^{-7}	2.0×10^{-9}	
JH10 vs *mhcA*$^{-}$/*mhcA*$^{+}$		NS	NS	NS	NS	1.6×10^{-3}	NS	
mhcA^{-}/*mhcA*$^{+}$ vs 3XALA		NS	NS	NS	NS	NS	3.6×10^{-3}	
mhcA^{-}/*mhcA*$^{+}$ vs 3XASP		3.1×10^{-9}	2.1×10^{-17}	2.3×10^{-10}	1.2×10^{-7}	1.4×10^{-3}	NS	

Values in the top half of the table are means±standard deviation.

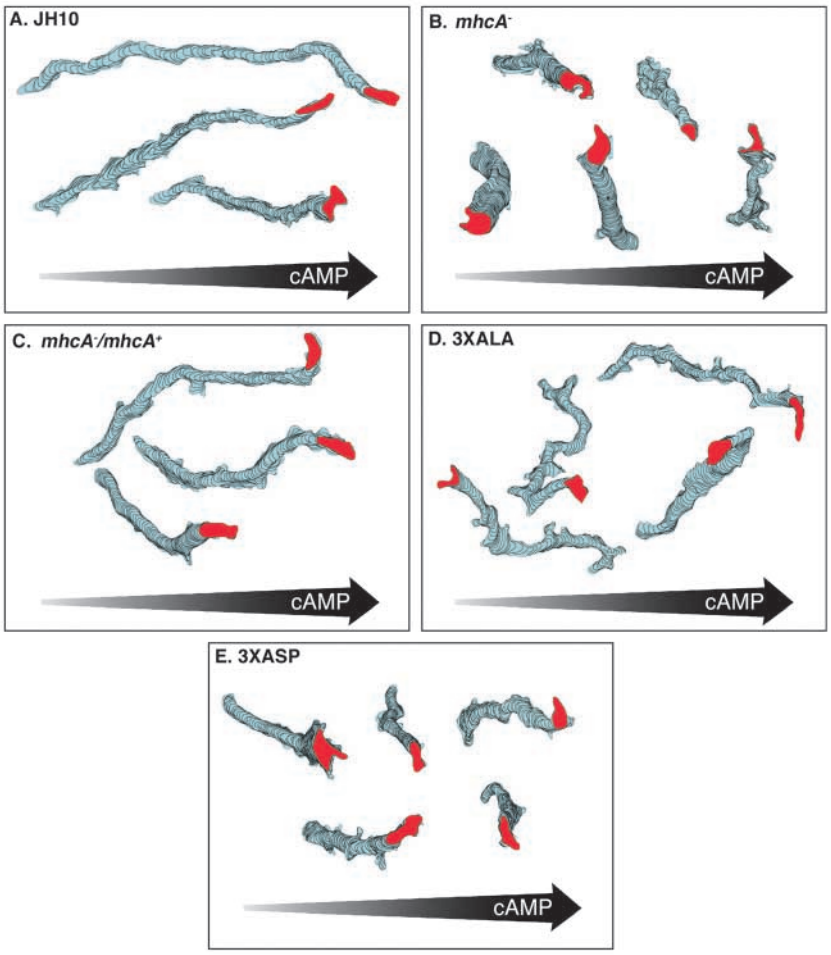

Fig. 5. Perimeter tracks of representative control and mutant cells translocating in a spatial gradient of cAMP, the direction of which is shown by the arrow in each panel. The red cell image represents the last one in each track. Cells were reconstructed at 8-second intervals.

that of the entire *mhcA*$^{-}$ population (+0.05±0.21 μm per minute), but still far below that of JH10 cells (+0.48±0.32 μm per minute) (Table 2). More significantly, 80% of the ten fastest *mhcA*$^{-}$ cells exhibited a positive chemotactic index, a proportion approaching that of JH10 cells (90%) (Table 2). Together, these results demonstrate that the fastest *mhcA*$^{-}$ cells do indeed show chemotaxis in a spatial gradient of cAMP, but with far less efficiency than JH10 cells.

Vector tracks and difference pictures provided a clue as to why the chemotactic efficiency of the fastest *mhcA*$^{-}$ cells was still far below that of JH10 cells. While sequential vectors of chemotaxing JH10 cells were uniformly aligned in the direction of persistent translocation (i.e. in the direction of the increasing gradient of cAMP) (Fig. 6A), the direction of sequential vectors of average *mhcA*$^{-}$ cells pointed in all directions (Fig. 6B). However, the vectors of the fastest *mhcA*$^{-}$ cells in a spatial gradient were loosely aligned in the direction of persistent translocation, constantly exhibiting small fluctuations in direction (Fig. 6C). These fluctuations suggested instability in the dominant anterior pseudopod. This suggestion was supported by a comparison of expansion zones in the corresponding difference pictures. While the major expansion zone (green) of JH10 cells were compact and restricted to the very anterior end of the elongate cell bodies (Fig. 6A), the expansion zones of fast, chemotaxing *mhcA*$^{-}$ cells (Fig. 6C) rimmed the perimeter of the anterior half of the cell body, changing shape continuously and frequently fragmenting into multiple expansion zones (Fig. 6C). These results support the conclusion that *mhcA*$^{-}$ cells were capable of anterior-posterior polarity, persistent translocation and chemotaxis in a spatial gradient of cAMP. However, they revealed that even when *mhcA*$^{-}$ cells extended an anterior pseudopod along the substratum in the direction of the increasing cAMP gradient and moved at instantaneous velocities greater than 4 μm per minute, most aspects of translocation were still defective and chemotaxis highly inefficient.

3XALA chemotaxis in a spatial gradient of cAMP

3XALA cells translocated in a spatial gradient of cAMP with mean instantaneous velocity, directional change and persistence values similar to that of *mhcA*$^{-}$/*mhcA*$^{+}$ cells (Table 2). In addition, both mean maximum length and roundness were similar to that of *mhcA*$^{-}$/*mhcA*$^{+}$ cells (Table 2). However, the chemotactic index of 3XALA cells was +0.22±0.48, less than half that of *mhcA*$^{-}$/*mhcA*$^{+}$ cells (+0.48±0.32), and the percentage of cells exhibiting a positive chemotactic index was 74%, compared to 85% for *mhcA*$^{-}$/*mhcA*$^{+}$ cells. (Table 2). Histograms revealed a far broader distribution of chemotactic indices than that of *mhcA*$^{-}$/*mhcA*$^{+}$ cells, with a significantly larger proportion in the negative range (data not shown). Hence, although 3XALA cells are as fast as control cells and chemotactically responsive, the efficiency of chemotaxis in a spatial gradient of cAMP was diminished. The reason for this was evident in perimeter tracks. The tracks of 3XALA cells (Fig. 5D) included more sharp turns than those of *mhcA*$^{-}$/*mhcA*$^{+}$ cells (Fig. 5C). As previously reported (Stites et al., 1998), these turns were the result of abnormal pseudopodial bifurcation, described in the 3D reconstructions of representative 3XALA cells in buffer (Fig. 4D). Vector tracks revealed that between turns, 3XALA cells (Fig. 6E) exhibited a level of persistence similar to that of *mhcA*$^{-}$/*mhcA*$^{+}$ cells (Fig. 6D). Difference pictures revealed anterior localization of expansion zones (Fig. 6E) similar to that of *mhcA*$^{-}$/*mhcA*$^{+}$ cells (Fig. 6D).

3XASP chemotaxis in a spatial gradient of cAMP

3XASP cells translocated in a spatial gradient of cAMP with reduced mean instantaneous velocity, like *mhcA*$^{-}$ cells (Table 2). The directional change parameter was higher and the persistence factor lower than that of *mhcA*$^{-}$/*mhcA*$^{+}$ cells, like

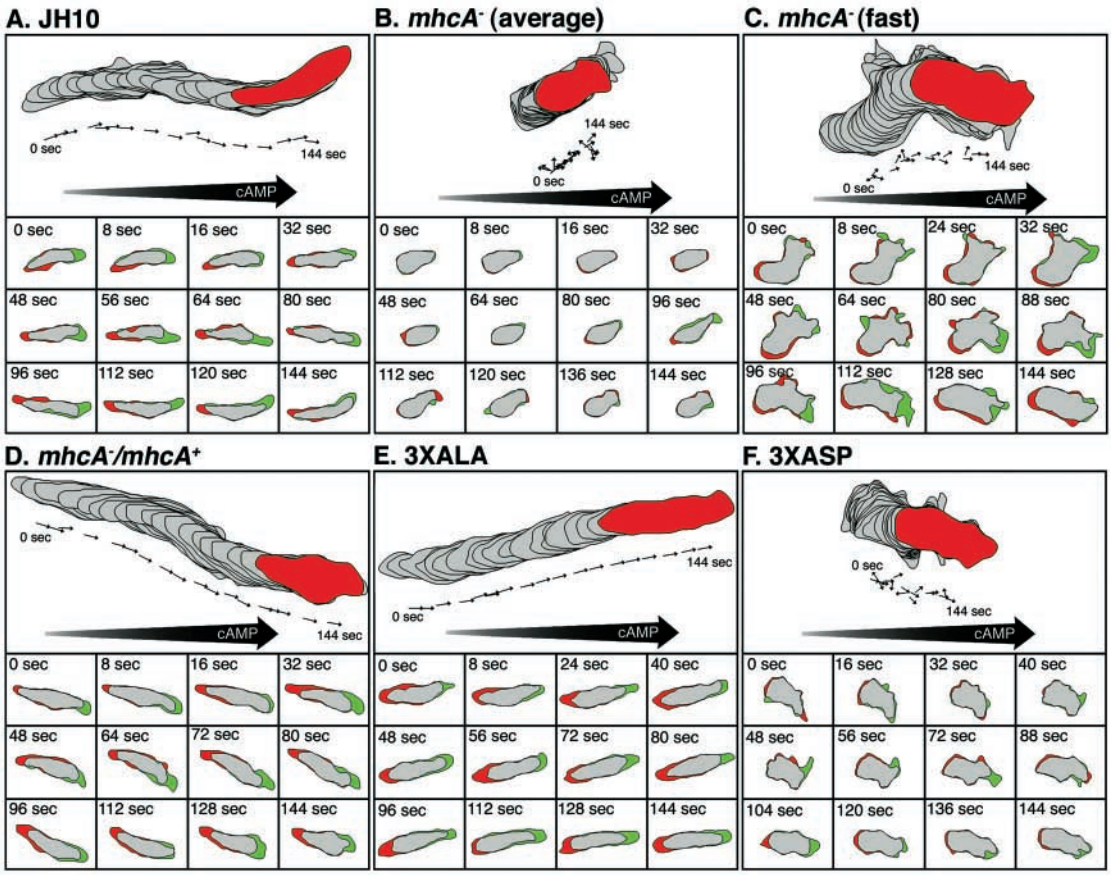

Fig. 6. A comparison of translocation of control and mutant cells in spatial gradients of cAMP. For each representative mutant cell, a perimeter track, vector track and set of difference pictures are presented. In perimeter tracks, the red image is the last in the sequence. Vectors were computed between centroids at 8-second intervals. Green and red zones of difference pictures indicate expansion and contraction zones, respectively.

mhcA⁻ cells (Table 2). In addition, mean length was reduced (Table 2). 3XASP cells did, however, exhibit a positive chemotactic index of +0.40±0.15 and a positive chemotaxis measure of 98%, values very close to control cells and significantly higher than that of *mhcA*⁻ cells (Table 2). Perimeter tracks of 3XASP cells in spatial gradients of cAMP were of similar lengths to those of *mhcA*⁻ cells, but were far more frequently in the direction of the spatial gradient (Fig. 5E). Vector tracks of average 3XASP cells translocating up a spatial gradient of cAMP (Fig. 6F), even though in the right direction, revealed directional instability similar to that of fast *mhcA*⁻ cells (Fig. 6C). Instability, as in buffer, corresponded to a less stable and less intact anterior pseudopod, as evidenced by the expansion zones in difference pictures (Fig. 6F). These results demonstrate that even though 3XASP cells were abnormally slow, they showed chemotaxis with a high level of efficiency in a spatial gradient of cAMP.

Mutant cell responses to temporal gradients of cAMP

To test responses to the temporal and concentration components of a natural wave, cells were treated with four consecutive temporal waves of cAMP generated in a perfusion chamber in the absence of established spatial gradients of cAMP (Varnum et al., 1985; Wessels et al., 1992; Zhang et al., 2002). As previously described for wild-type cells, JH10 cells responded to the increasing temporal gradient of cAMP in the front of each of the last three in a series of four waves with a transient velocity surge (Fig. 7A). The frequency of surges in the front of the last three in a series of four waves was over 68% (30 cells analyzed). Difference pictures revealed that in the front of the wave, cells were elongate, with a localized anterior expansion zone, at the peak of the wave, cells stopped extending pseudopods and became less elongate, and in the back of the wave, cells again extended pseudopods, but in an apolar fashion, and did not elongate (Fig. 7A), as previously described for wild-type cells (Soll et al., 2003; Varnum et al., 1985; Wessels et al., 1992; Zhang et al., 2002). By contrast, *mhcA*⁻ cells did not respond with velocity surges to the increasing temporal gradient of cAMP in the front of each of the last three in a series of four temporal waves (20 cells analyzed) (Fig. 7B). Difference pictures in the front, peak and back of the third in a series of four waves were indistinguishable, revealing no changes in pseudopod dynamics, cell shape or polarity (Fig. 7B).

Cells of control strain *mhcA*⁻/*mhcA*⁺ surged in the front of the last three of four consecutive temporal waves (data not shown), like JH10 cells (Fig. 7A). The frequency of surges,

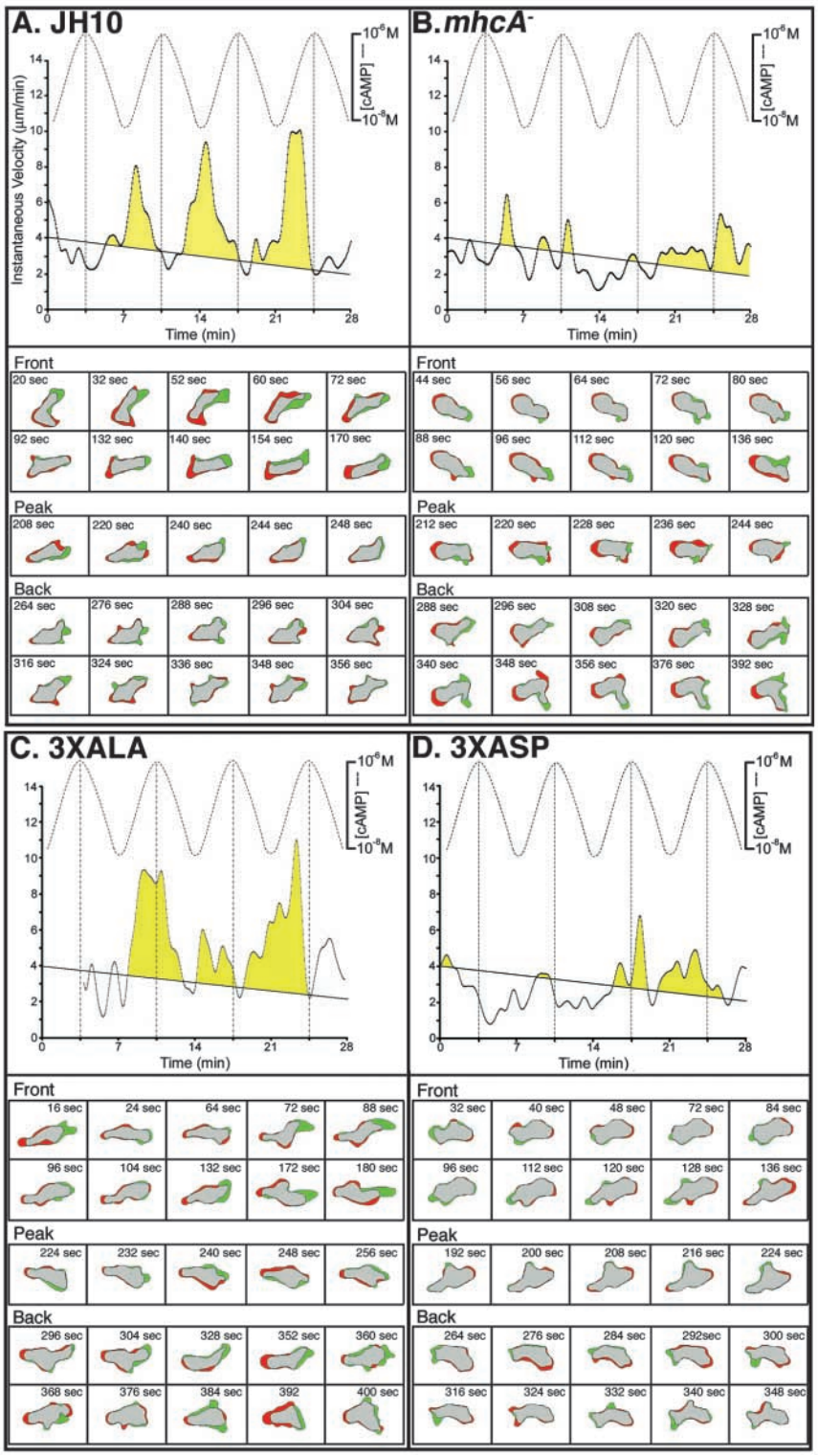

Fig. 7. The behavior of a representative JH10 cell (A), *mhcA*$^{-}$ cell (B), 3XALA cell (C) and 3XASP cell (D) in a series of four simulated temporal waves of cAMP. Instantaneous velocity of each cell is plotted as a function of time for each cell. The estimated waves of cAMP are plotted at the top. Difference pictures are presented for each cell in the front, peak and back of the third wave. Velocity above an arbitrary threshold line drawn from 4 to 2 μm per minute over the 28-minute period of analysis was color-coded yellow to accentuate the velocity surges in response to the front of the second, third and fourth wave for JH10 and 3XALA cells, but not for *mhcA*$^{-}$ and 3XASP cells. In difference pictures, expansion zones are color-coded green and contraction zones red.

however, was approximately 58% (30 cells analyzed), slightly lower than that of JH10 cells. Difference pictures revealed an elongate cell shape and a compact apical pseudopod in the front of the wave, a decrease in cell elongation and suppression of anterior pseudopod extension at the peak of the wave, and apolar pseudopod expansion in the back of the wave (data not shown). 3XALA cells exhibited velocity surges in the front of the last three in a series of four waves (Fig. 7C), but the frequency was approximately 51% (30 cells analyzed), slightly lower than that of *mhcA*$^{-}$/*mhcA*$^{+}$ cells. 3XALA cells were elongate in the front of the wave, rounder at the peak of the wave, and extended pseudopods in an apolar fashion in the back of the wave (Fig. 7C), like JH10 (Fig. 7A) and *mhcA*$^{-}$/*mhcA*$^{+}$ (data not shown) cells. In marked contrast to 3XALA cells, 3XASP cells did not surge in the front of the last three in a series of four waves (Fig. 7D), and did not exhibit the changes in shape, pseudopod dynamics and polarity associated with the three phases of the wave (Fig. 7D). In all respects, 3XASP cells behaved like *mhcA*$^{-}$ cells in the three phases of a temporal wave.

Chemotactic responses to natural waves in mixed cultures

Based on the observed behaviors in buffer, and in spatial and temporal gradients of cAMP, one might expect 3XALA, but not *mhcA*$^{-}$ or 3XASP cells, to be chemotactically responsive to natural waves of cAMP generated by control cells in mixed aggregation territories. To test this, mutant cells vitally stained with DiI were mixed with JH10 cells at a ratio of 1:9, respectively. Transmitted images (all cells) and fluorescent images (only mutant cells) were simultaneously acquired. DiI-stained *mhcA*$^{-}$ cells mixed with JH10 cells did not exhibit velocity surges like neighboring JH10 cells in the fronts of successive waves of cAMP relayed outwardly from the aggregation center through the aggregation territory (Fig. 8A). Centroid tracks revealed that *mhcA*$^{-}$ cells made no net progress towards the aggregation center, in contrast to neighboring JH10 cells (Fig. 8B). Similar results were obtained for 3XASP cells mixed with JH10 cells (Fig. 8C and D, respectively). In marked contrast, 3XALA cells similarly mixed with JH10 cells surged synchronously with neighboring JH10 cells in response to successive natural waves of cAMP relayed by the majority JH10 cells (Fig. 8E). Centroid tracks in this case revealed that 3XALA cells

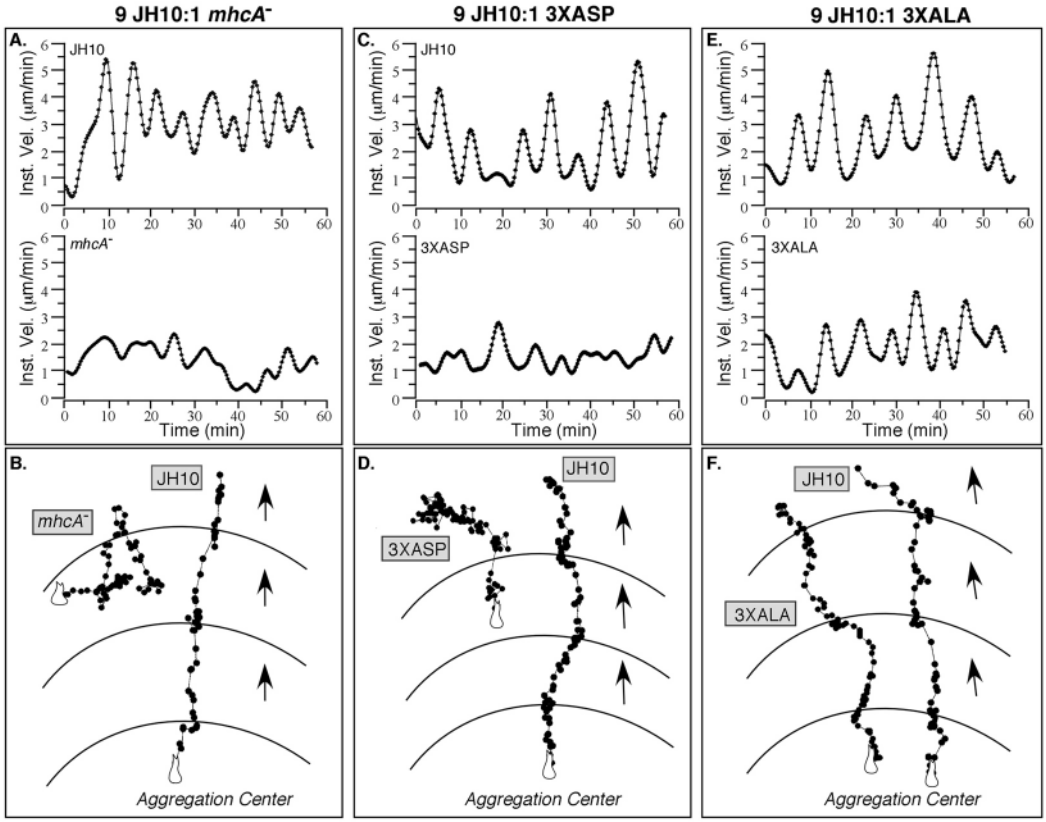

Fig. 8. *mhcA*$^{-}$ and 3XASP cells are incapable, while 3XALA cells are capable, of chemotaxis in natural waves of cAMP relayed through an aggregation territory of control cells. *mhcA*$^{-}$, 3XASP or 3XALA cells were mixed with control (JH10) cells at a ratio of 1:9 and examined early in the aggregation process, during the single cell chemotaxis stage. *mhcA*$^{-}$ cells in each case were stained with DiI before mixing, while control cells were unstained. Transmitted and fluorescent images were simultaneously collected at 20-second intervals. (A,C,E) Instantaneous velocity of a control and mutant cell in the same neighborhood (within 15 μm) as a function of time. (B,D,F) Centroid plots of neighboring control and mutant cells in the aggregation territory. The aggregation center is at the bottom. Curved lines represent the peaks of sequential waves interpreted from control centroid plots.

made net progress towards an aggregation center, like neighboring JH10 cells (Fig. 8F).

Aggregation in homogeneous cultures

While cells of both control strains (JH10, *mhcA*$^{-}$/*mhcA*$^{+}$), in homogeneous monolayers on agar, streamed late in aggregation into large aggregates (Fig. 9A and B, respectively), cells of *mhcA*$^{-}$ and 3XASP formed large numbers of aggregates in the absence of streaming (data not shown). Homogeneous populations of 3XALA cells plated on an agar surface also underwent aberrant aggregation. 3XALA cells (Fig. 9C) formed no streams or highly truncated streams, resulting in an increased number of very small aggregates. This was indeed an unexpected result since 3XALA cells appeared to respond normally to natural waves of cAMP relayed by JH10 cells in mixed cultures (Fig. 8E,F). We therefore tested whether 3XALA cells were defective in entering streams by mixing DiI-labeled 3XALA cells with unlabeled JH10 cells at a ratio of 1:9, respectively, and monitoring their behavior late in the aggregation process using simultaneous bright-field (all cells) and laser scanning confocal microscopy (only DiI-stained cells). While the majority of JH10 cells readily entered streams, DiI-labeled 3XALA cells had problems doing so (Fig. 9D). 3XALA cells remained at the edges of streams and failed to form end-to-end contacts (Fig. 9D).

The role of MHC phosphorylation in F-actin localization during chemotaxis

Our behavioral studies, therefore, revealed specific defects in chemotaxis in the three mutants analyzed. We next tested whether these defects were associated with defects in the reorganization of F-actin during chemotaxis (Wessels et al., 2004), by staining cells migrating in buffer or responding to the increasing and decreasing temporal gradients of cAMP in the front and back of a wave, respectively, with Oregon Green-conjugated phalloidin. In all cell types migrating in buffer, F-actin was localized predominantly in pseudopods (Fig. 10A,D,G,J). A low level of F-actin was distributed throughout the nonpseudopodial cytoplasm. To analyze the changes in F-actin localization in the cytoplasm and cortex, line plots of staining intensity were generated from LSCM scans taken 1 μm above the substratum. The line plots were computed across cell bodies below the nucleus (white line in the second of each three panel set, Fig. 10A-L). For *mhcA*$^{-}$/*mhcA*$^{+}$ cells in buffer,

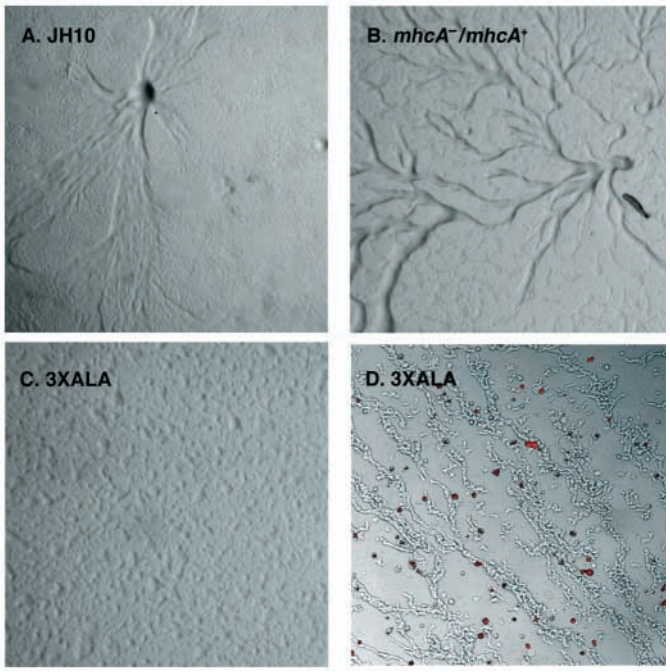

Fig. 9. 3XALA cells exhibit aberrant streaming and also have problems entering streams of control cells. (A) Streaming during late aggregation of JH10 cells on agar. (B) Streaming during late aggregation of *mhcA*$^{-}$/*mhcA*$^{+}$ cells on agar. (C) Late aggregation of 3XALA cells on agar. (D) DiI-labeled 3XALA cells (red) mixed with unlabeled JH10 cells at a ratio of 1:9 failed to enter JH10 streams. Stained and unstained cells were co-imaged with simultaneous bright-field optics and laser scanning confocal microscopy.

the line plots revealed low level staining through the cytoplasm and cortex. Cortical staining at the two ends of the line plot was on average slightly higher than staining through the cytoplasm, as suggested in Fig. 10A. The average intensity ratio of cortical to cytoplasmic staining of *mhcA*$^{-}$/*mhcA*$^{+}$ cells in buffer was 1.1 (n=10). In response to the increasing temporal gradient of cAMP in the front of the third in a series of four simulated temporal waves, the level of F-actin staining in control cells more than doubled in the cytoplasm and more than quadrupled in the cortex (Fig. 10B, two examples). In response to the decreasing temporal gradient of cAMP in the back of a temporal wave, the levels of F-actin in the cytoplasm and cortex returned again to that in buffer (Fig. 10C). Similar results were obtained for 20 additional *mhcA*$^{-}$/*mhcA*$^{+}$ cells in the front and back of simulated temporal waves of cAMP. Similar results were also recently reported for JH10 cells in buffer, in the front and in the back of temporal waves of cAMP (Wessels et al., 2004).

In *mhcA*$^{-}$ and 3XASP cells migrating in buffer, line plots revealed that the level of F-actin was low in both *mhcA*$^{-}$ and 3XASP cells in the cytoplasm and cortex (Fig. 10D and J, respectively), as in control cells (Fig. 10A). In contrast to control cells, however, the increasing temporal gradient of cAMP in the front of a wave did not stimulate increases in cytoplasmic or cortical F-actin in either *mhcA*$^{-}$ cells (Fig. 10E) or 3XASP cells (Fig. 10K). In *mhcA*$^{-}$ and 3XASP cells, the pattern of F-actin distribution remained constant in buffer, in the increasing temporal gradients of cAMP in the front of the wave and in the decreasing temporal gradient of cAMP in the back of the wave (Fig. 10D,E,F, respectively, for *mhcA*$^{-}$ and J,K,L, respectively, for 3XASP).

Line scans revealed low levels of F-actin in the cytoplasm and cortex of 3XALA cells in buffer (Fig. 10G) comparable to that in *mhcA*$^{-}$/*mhcA*$^{+}$ cells (Fig. 10A). In response to the increasing temporal gradient of cAMP in the front of a temporal wave, the level of cytoplasmic F-actin more than doubled (Fig. 10H), as in *mhcA*$^{-}$/*mhcA*$^{+}$ cells (Fig. 10B), but the level of F-actin in the cortex did not quadruple (Fig. 10H), in marked contrast to control cells (Fig. 10B). In response to the decreasing temporal gradient of cAMP in the back of a temporal wave, the level of F-actin in the cytoplasm returned to that in buffer (Fig. 10I), as it did in *mhcA*$^{-}$/*mhcA*$^{+}$ cells (Fig. 10C). Hence, while neither *mhcA*$^{-}$ nor 3XASP cells exhibited the normal increases in cytoplasmic and cortical F-actin in response to the front of the wave, 3XALA cells exhibited the cytoplasmic, but not the cortical increase. These results were verified in independent preparations.

Discussion

Cells lacking MHC still can do some things

Before assessing the role of MHC phosphorylation through the computer-assisted analysis of the 3XALA and 3XASP mutants, we re-analyzed the behavioral capabilities of cells lacking MHC using the higher resolution computer-assisted systems and experimental protocols developed since the original study in 1988 (Wessels et al., 1988). *mhcA*$^{-}$ cells were found to be capable of polarization (i.e. distinguishing between anterior and posterior ends), extending a dominant anterior pseudopod, translocating in a persistent fashion and chemotaxis up a spatial gradient of cAMP. However, all of these behaviors were very poorly executed. *mhcA*$^{-}$ cells could not properly elongate and had a hard time maintaining a single dominant pseudopod, or extending it along the substratum. The majority of *mhcA*$^{-}$ cells were mound-shaped and extended their major pseudopod dorsally rather than along the substratum, and even when they accomplished this, the cell body was abnormally short and the pseudopod abnormally broad, continually changing shape and fragmenting. Small pseudopods also formed from the lateral and dorsal surfaces of the cell. It was evident from the behavior of *mhcA*$^{-}$ cells that myosin II is essential for (1) normal cell elongation, (2) normal pseudopod extension along the substratum, (3) maintenance of a compact dominant pseudopod, (4) attaining normal velocity, and (4) attaining normal chemotactic efficiency in a spatial gradient of cAMP. *mhcA*$^{-}$ cells did not respond at all to increasing and decreasing temporal gradients in a series of four simulated temporal waves, indicating that those responses were completely dependent on MHC and, hence, a functional myosin II. These results are consistent with several earlier observations on the behavior of other *mhcA* null or down-regulated mutants. Wessels et al. (Wessels et al., 1988) in an earlier study demonstrated that cells lacking MHC were rounder, slower and chemotactically compromised. Peters et al. (Peters et al., 1988) demonstrated that *mhcA*$^{-}$ cells accumulated cAMP receptors on the cell surface during development, and exhibited normal increases in cAMP, cGMP and F-actin in the cytoskeleton in response to 2′-deoxy-cAMP

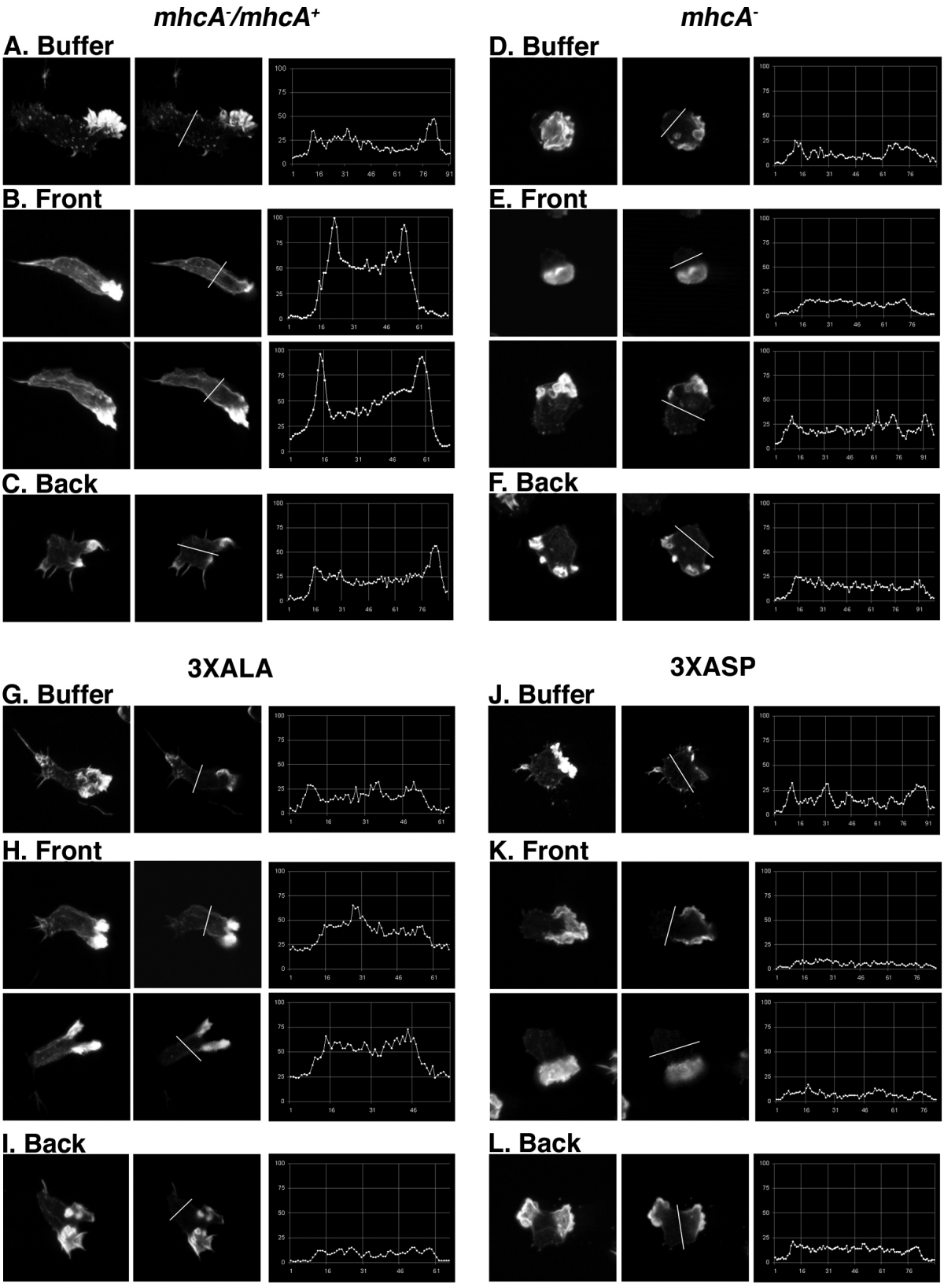

Fig. 10. F-actin localization analyzed by Oregon-Green-phalloidin staining in *mhcA*$^{-}$/*mhcA*$^{+}$, *mhcA*$^{-}$, 3XALA and 3XASP cells in buffer, in response to the increasing temporal gradient of cAMP in the third in a series of four temporal and in response to the decreasing temporal gradient of cAMP in the back of the wave. For each representative cell, the first panel contains a projection image through all laser scanning confocal microscope (LSCM) sections, the second panel contains a single LSCM section at 1 μm above the substratum, and the third panel is a line plot of staining intensity in the single LSCM section across the cell behind the nucleus (indicated by the white line in the second panel).

added to cells in buffer. Peters et al. (Peters et al., 1988) also demonstrated in a qualitative droplet assay that *mhcA*$^-$ cells exhibited a positive chemotactic response to 2′-deoxy-cAMP. Finally, Knecht and co-workers (Sheldon and Knecht, 1996) obtained side view images of *mhcA*$^-$ cells in buffer, which also revealed a mound-shaped cell body and dominant pseudopods forming from the dorsal cell surface. Together, these studies demonstrate that while myosin II heavy chain is not essential for cell polarization, cellular translocation and chemotaxis in a spatial gradient of cAMP, it plays a critical role in fine-tuning all of these processes. Furthermore, studies described here demonstrate that myosin II heavy chain is essential for responding to the temporal gradients of cAMP associated with the front and back of natural waves. It was, therefore, not surprising to find that *mhcA*$^-$ cells could not move towards an aggregation center in response to natural waves of cAMP relayed by a majority of control cells in a mixed aggregation territory.

3XASP: constitutively phosphorylated MHC

Several lines of evidence suggest that the MHC of 3XASP cells mimics the constitutively phosphorylated state. First, biochemical analyses of myosin II purified from 3XASP revealed that assembly was defective in vitro (Egelhoff et al., 1993), as was observed when phosphorylation of MHC inhibited filament formation in vitro (Kuczmarski and Spudich, 1980; Coté and McCrea, 1984; Ravid and Spudich, 1989). Second, the developmental phenotype of 3XASP cells is remarkably similar to that of *mhcA*$^-$ cells, as well as myosin heavy chain kinase (MHCK)-overexpressing cells (Egelhoff et al., 1993; Manstein et al., 1989; Rico and Egelhoff, 2003). Finally, electron microscopy revealed that the majority of 3XASP myosin II molecules are in the bent configuration (Liang et al., 1999), which is consistent with the constitutive phosphorylated state. Hence, the myosin II of 3XASP cells should and does localize to the cytoplasm rather than cortex (Egelhoff et al., 1996). 3XASP cells, like *mhcA*$^-$ cells, were abnormally slow. They also formed abnormal pseudopods that changed shape and fragmented. However, the defects of 3XASP cells, shared with *mhcA*$^-$ cells, were less severe, suggesting either that unpolymerized 3XASP myosin II can perform a portion of polymerized myosin II function, that myosin II mimicking the phosphorylated state may still polymerize at low levels, resulting in partial function, or that 3XASP MHC, despite displaying many of the characteristics of phosphorylated wild-type MHC, does not completely mimic the phosphorylated state. To our surprise, 3XASP cells were relatively efficient at chemotaxis in a spatial gradient of cAMP. However, 3XASP cells, like *mhcA*$^-$ cells, did not respond to the increasing and decreasing temporal gradients of cAMP associated with the front and back, respectively, of a wave, and could not move chemotactically towards an aggregation center in response to waves of cAMP relayed by a majority of control cells in a mixed aggregation territory. These results indicate that MHC must either be in the unphosphorylated state or must be able to undergo dephosphorylation in order for a cell to elongate along the substratum properly, extend a compact, dominant, anterior pseudopod, attain the translocation speed of wild-type cells, undergo efficient chemotaxis in a spatial gradient of cAMP, and respond to the temporal gradients of cAMP associated with the front and back of the wave. Presumably, to do all of these things, a cell needs normal levels of cortical tension.

3XALA, constitutively unphosphorylated MHC

Egelhoff et al. (Egelhoff et al., 1996) demonstrated that cortical tension is abnormally elevated in 3XALA cells. Increased cortical tension presumably results from the over-assembly in the cortex of constitutively unphosphorylated MHC (Levi et al., 2002). In spite of this, 3XALA cells were normal in most aspects of basic motile behavior and in most aspects of single cell chemotaxis. In buffer, they moved with the speed, directionality and persistence of control cells, although they were on average a bit rounder, apparently a result of increased cortical tension and cyclic bifurcation of the anterior pseudopod, the latter characteristic previously reported by Stites et al. (Stites et al., 1998). In a spatial gradient of cAMP, 3XALA cells did show chemotaxis, but did so with a reduction in efficiency, presumably a consequence of pseudopod bifurcation, which forces turns. 3XALA cells responded normally to temporal gradients of cAMP and surged normally towards aggregation centers in the front of cAMP waves relayed by the majority control cells in mixed cultures. Together, the in vitro behavior studies suggested an unexpected level of normality for a cell that could not undergo MHC phosphorylation. However, aggregates formed by homogeneous lawns of 3XALA cells were smaller than control cell aggregates and streaming was almost non-existent, suggesting that MHC phosphorylation was critical for the later stages of natural aggregation. Mixing experiments in which 3XALA cells were selectively stained revealed that 3XALA cells localized to streams of majority control cells, but could not integrate into them, and hence remained on the surfaces of natural streams.

A specific 3XALA defect in F-actin localization in the front of the wave

In buffer, F-actin localizes in the pseudopods of control cells, but is distributed at much lower levels throughout the cytoplasm and cortex. In response to an increasing temporal gradient of cAMP, while the majority of F-actin still remains localized in pseudopodia, there is more than a doubling of F-actin in the cytoplasm and more than a quadrupling of F-actin in the cortex (Wessels et al., 2004), as illustrated in Fig. 11A. In both *mhcA*$^-$ and 3XASP cells in buffer, the distribution of F-actin is similar to that of control cells. However, in contrast to control cells, there is neither a doubling of F-actin in the cytoplasm nor a quadrupling of F-actin in the cortex in response to an increasing temporal gradient of cAMP in the front of a simulated temporal wave, as shown diagrammatically in Fig. 11B. These results demonstrate that the increases in cytoplasmic and cortical F-actin in response to the increasing temporal gradient of cAMP in the front of the wave require either unphosphorylated MHC or the actual event of MHC dephosphorylation.

In 3XALA cells translocating in buffer, the distribution of F-actin is also similar to that of control cells. In an increasing temporal gradient of cAMP, the level of cytoplasmic F-actin in 3XALA cells more than doubles (Fig. 11C), just as it does in

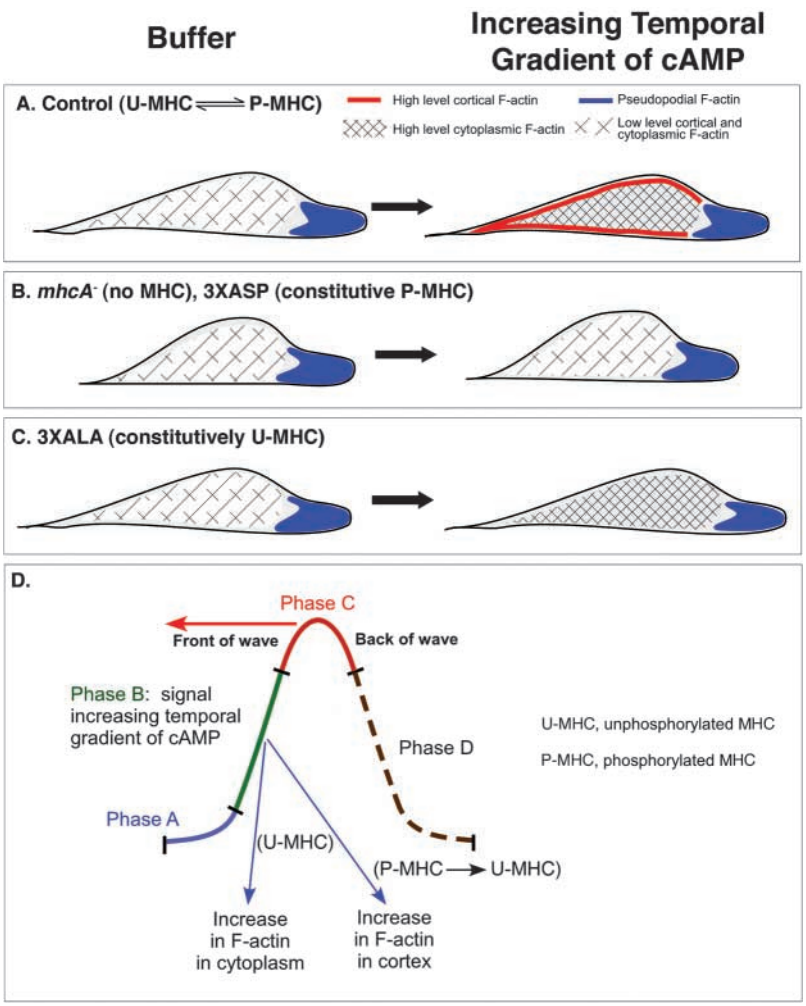

Fig. 11. Diagrams of F-actin localization in (A) control and (B) *mhcA*$^{-}$ or 3XASP and (C) 3XALA cells in buffer and in response to the increasing temporal wave of cAMP in the front of a wave. (D) Model of the regulation of F-actin localization in the cytoplasm and cortex in response to the increasing gradient of cAMP in the front of a wave.

control cells (Fig. 11A). This specific result, together with the absence of an increase in cytoplasmic F-actin in 3XASP cells, suggests that the normal increase in cytoplasmic F-actin in response to an increasing temporal gradient of cAMP is dependent upon the presence of unphosphorylated MHC, not upon the actual process of MHC dephosphorylation. However, in contrast to control cells (Fig. 11A), the level of F-actin in 3XALA cells does not quadruple in the cortex in response to an increasing temporal gradient of cAMP (Fig. 11C). This result, together with the absence of an increase in 3XASP cells, suggests that the normal increase in cortical F-actin, in contrast to the increase in cytoplasmic F-actin, depends upon the dephosphorylation of MHC, not upon the presence of unphosphorylated MHC. Mechanistically, this suggests, without biochemical evidence, that unphosphorylated, unpolymerized myosin may bind to F-actin, then polymerize in the cortex, carrying with it F-actin. This dissociation of dependencies is shown diagrammatically in Fig. 11D. However, the possibility must also be entertained that overpolyermization of myosin II in the cortex of 3XALA cells (Egelhoff et al., 1993) may physically prevent F-actin from localizing in the cortex, perhaps by interfering with actin-membrane interactions. This seems unlikely in light of our findings that F-actin does not localize to the cortex of 3XASP cells in the front of the wave. Given that myosin II does not assemble in the cortex of 3XASP cells, the absence of F-actin localization cannot be due to a physical barrier to actin assembly.

Levi et al. (Levi et al., 2002) demonstrated that the localization of myosin II to the cortex in response to chemoattractant depends upon the presence of filamentous F-actin. They found that when 10^{-4} M cAMP was rapidly added to aggregation-competent cells suspended in buffer, myosin localized to the cortex within seconds. However, when latrunculin A, which depolymerizes F-actin, was added to cultures prior to the addition of cAMP, myosin II did not localize to the cortex upon cAMP treatment. Although the rapid application of cAMP to cells is distinct from the normal increase in cAMP in the front of a natural wave, the results of Levi et al. (Levi et al., 2002) combined with those presented here, lend support to our suggestion that polymerized F-actin may interact with dephosphorylated, unpolymerized MHC in receptor-mediated cortical colocalization.

MHC phosphorylation as a target in chemotactic regulation

We previously demonstrated through analysis of the mutant S13A, which expresses a constitutively unphosphorylated myosin II regulatory light chain (RLC), that either the process of RLC phosphorylation or the presence of phosphorylated RLC is necessary first for normal lateral pseudopod formation and, second, for the normal behavioral responses to the high concentration of cAMP at the peak of the wave and the decreasing temporal gradient of cAMP in the back of the wave (Zhang et al., 2002). Recently, we demonstrated that the *rasC* null mutant exhibited the same behavioral defects at the peak and in the back of the wave as S13A, suggesting that RasC functions upstream of regulatory light chain phosphorylation in these two phases of the wave (Wessels et al., 2004). The comparable constitutively unphosphorylated MHC mutant 3XALA shares none of the phenotypic characteristics of S13A during basic motile behavior in the absence of signal, or in the peak and back of the wave. It does not appear to suppress normal lateral pseudopods under all conditions, as does S13A, it rounds up at the peak of the wave, in contrast to S13A, and it becomes apolar in the back of the wave, in contrast to S13A. Hence, even though early experiments indicated that the cAMP signal may stimulate phosphorylation of the two associated molecules in a coordinate fashion (Berlot et al., 1985; Berlot et al., 1987), the functional roles of phosphorylation of the two are disparate.

The most dramatic defect exhibited by 3XALA was the absence of the cortical localization of F-actin in response to the increasing temporal gradient of cAMP in the front of the wave.

Unfortunately, this increase has only recently been documented (Wessels et al., 2004), and has not been tested in other mutants in which there is a behavioral defect in the front of the wave, such as *regA*$^{-}$ (Wessels et al., 2000) or *myoA*$^{-}$/*myoF*$^{-}$ (Falk et al., 2003). In addition, the defect of 3XALA cells in entering streams is poorly understood because the behavior of cells during streaming has not been subjected to rigorous computer-assisted analysis (Soll et al., 2003) or tested for in other mutants. Therefore, although it seems likely that the phosphorylation-dephosphorylation of MHC will prove to be targets of one or more regulatory cascades emanating from the different phases of the wave (Soll et al., 2003), as has been proved to be the case for the phosphorylation-dephosphorylation of RLC, further experiments must now be performed to identify these connections.

The research described here was supported by National Institutes of Health grant HD-18577. P.H. was supported by a postdoctoral fellowship from the American Cancer Society (grant PF-01-110-01-CSM). The authors thank D. J. Manstein and T. T. Egelhoff for sharing mutants.

References

Berlot, C. H., Spudich, J. A. and Devreotes, P. N. (1985). Chemoattractant-elicited increases in myosin phosphorylation in *Dictyostelium*. *Cell* **43**, 307-314.

Berlot, C. H., Devreotes, P. N. and Spudich, J. A. (1987). Chemoattractant-elicited increases in *Dicytostelium* myosin phosphorylation are due to changes in myosin localization and increases in kinase activity. *J. Biol. Chem.* **262**, 3918-3926.

Bjerrum, O. J. and Schafer-Nielsen, C. (1986). *Analytical electrophoresis* (ed. M. J. Dunn), p. 315. Weinheim, Germany: Verlag Chemise.

Bradford, M. M. (1976). A rapid sensitive method for the quantization of microgram quantities of protein utilizing the principle of protein-dye binding. *Anal. Biochem.* **72**, 248-254.

Côté, G. P. and McCrea, S. M. (1987). Selective removal of the carboxyl-terminal tail end of the *Dictyostelium* myosin II heavy chain by chymotrypsin. *J. Biol. Chem.* **262**, 13033-13038.

De Lozanne, A. and Spudich, J. A. (1987). Disruption of the *Dictyostelium* myosin heavy chain gene by homologous recombination. *Science* **236**, 1086-1091.

Egelhoff, T. T., Lee, R. J. and Spudich, J. A. (1993). *Dictyostelium* myosin heavy chain phosphorylation sites regulate myosin filament assembly and localization in vivo. *Cell* **75**, 363-371.

Egelhoff, T. T., Nasmyth, T. V. and Brozovich, F. V. (1996). Myosin-based cortical tension in *Dictyostelium* resolved into heavy and light chain-regulated components. *J. Muscle Res. Cell Motil.* **17**, 269-274.

Falk, D. L., Wessels, D., Jenkins, L., Pham, T., Kuhl, S., Titus, M. A. and Soll, D. R. (2003). Shared, unique and redundant functions of three members of the class I myosins (MyoA, MyoB and MyoF) in motility and chemotaxis in *Dictyostelium*. *J. Cell. Sci.* **116**, 3985-3999.

Fukui, Y. (1990). Actomyosin organization in mitotic *Dictyostelium* amoebae. *Ann. N.Y. Acad. Sci.* **582**, 156-165.

Fukui, Y., Yumura, S. and Yumura, T. K. (1987). Agar-overlay immunofluorescence: high-resolution studies of cytoskeletal components and their changes during chemotaxis. *Methods Cell Biol.* **28**, 347-356.

Geiger, J., Wessels, D. and Soll, D. R. (2003). Human PMNs respond to temporal waves of chemoattractant like *Dictyostelium*. *Cell Motil. Cytoskeleton* **56**, 27-44.

Kessin, R. H. (2001). *Dictyostelium: Evolution, Cell Biology and the Development of Multicellularity*. Cambridge, UK: Cambridge University Press.

Khosla, M., Spiegelman, G. B., Insall, R. and Weeks, G. (2000). Functional overlap of the *Dictyostelium* RasG, RasD and RasB proteins. *J. Cell Sci.* **113**, 1427-1434.

Knecht, D. A. and Loomis, W. F. (1987). Antisense RNA inactivation of myosin heavy chain gene expression in *Dictyostelium discoideum*. *Science* **236**, 1081-1086.

Kuczmarski, E. R. and Spudich, J. A. (1980). Regulation of myosin self-assembly: phosphorylation of *Dictyostelium* heavy chain inhibits formation of thick filaments. *Proc. Natl. Acad. Sci. USA* **77**, 7292-7296.

Kuspa, A. and Loomis, W. F. (1994). Transformation of *Dictyostelium* – gene disruptions, insertional mutagenesis, and promoter traps. *Methods Mol. Genet.* **3**, 3-21.

Laemmli, U. K. (1970). Cleavage of structural proteins during the assembly of the head of the bacteriophage T4. *Nature* **227**, 592-596.

Levi, S., Polyakov, M. and Egelhoff, T. T. (2002). Myosin II dynamics in *Dictyostelium*: determinants for filament assembly and translocation to the cell cortex during chemoattractant responses. *Cell Motil. Cytoskeleton* **53**, 177-188.

Liang, W., Warrick, H. M. and Spudich, J. A. (1999). A structural model for phosphorylation control of *Dictyostelium* myosin II thick filament assembly. *J. Cell Biol.* **147**, 1039-1048.

Lockhart, S. R., Daniels, K. J., Zhao, R., Wessels, D. and Soll, D. R. (2003). Cell biology of mating in *Candida albicans*. *Eukaryot. Cell* **2**, 49-61.

Luck-Vielmetter, D., Schleicher, M, Rabaptin, B., Wippler, J. and Gerisch, G. (1990). Replacement of threonine residues by serine and alanine in a phosphorylatable heavy chain fragment of *Dictyostelium* myosin II. *FEBS Lett.* **269**, 239-243.

Manstein, D. J., Titus, M. A., DeLozanne, A. and Spudich, J. A. (1989). Gene replacement in *Dictyostelium*: generation of myosin null mutants. *EMBO J.* **8**, 923-932.

Moores, S. L., Fabry, J. H. and Spudich, J. A. (1996). Myosin dynamics in live *Dicytostelium* cells. *Proc. Natl. Acad. Sci. USA* **93**, 443-446.

Ostrow, B. D., Chen, P. and Chisholm, R. L. (1994). Expression of a myosin regulatory light chain phosphorylation site mutant complements the cytokinesis and developmental defects of *Dictyostelium* RMLC null cells. *J. Cell Biol.* **127**, 1945-1955.

Peters, D. J. M., Knecht, D. A., Loomis, W. F., Lozanne, A. D., Spudich, J. A. and van Haastert, P. J. M. (1988). Signal transduction, chemotaxis and cell aggregation in *dicytostelium discoideum* cells without myosin heavy chain. *Dev. Biol.* **128**, 158-163.

Ravid, S. and Spudich, J. A. (1989). Myosin heavy chain kinase from developed *Dictyostelium* cells. Purification and characterization. *J. Biol. Chem.* **264**, 15144-15150.

Rico, M. and Egelhoff, T. T. (2003). Myosin heavy chain kinase b participates in the regulation of myosin assembly into the cytoskeleton. *J. Cell Biochem.* **88**, 521-532.

Sheldon, E. and Knecht, D. A. (1996). *Dictyostelium* cell shape generation requires myosin II. *Cell Motil. Cytoskeleton* **35**, 59-67.

Shutt, D. C., Jenkins, L. M., Carolan, E., Stapleton, J., Daniels, K., Kennedy, R. and Soll, D. R. (1998). T cell syncytia induced by HIV release T cell chemoattractants: demonstration with a newly developed single cell chemotaxis chamber. *J. Cell Sci.* **111**, 99-109.

Soll, D. R. (1979). Timers in developing systems. *Science* **203**, 841-849.

Soll, D. R. (1988). "DMS", a computer-assisted system for quantitating motility, the dynamics of cytoplasmic flow and pseudopod formation: its application to *Dictyostelium* chemotaxis. *Cell Motil. Cytoskeleton* **10**, 91-106.

Soll, D. R. (1995). The use of computers in understanding how animal cells crawl. *Int. Rev. Cytol.* **163**, 43-104.

Soll, D. R. and Voss, E. (1998). Two and three dimensional computer systems for analyzing how cells crawl. In *Motion Analysis of Living Cells* (ed. D. R. Soll and D. Wessels), pp. 25-52. Sussex, UK: John Wiley.

Soll, D. R., Voss, E., Varnum-Finney, B. and Wessels, D. (1988). 'Dynamic Morphology System': a method for quantitating changes in shape, pseudopod formation and motion in normal mutant amoebae of *Dictyostelium discoideum*. *J. Cell. Biochem.* **37**, 177-192.

Soll, D. R., Voss, E., Johnson, O. and Wessels, D. (2000). Three-dimensional reconstruction and motion analysis of living, crawling cells. *Scanning* **22**, 249-257.

Soll, D. R., Wessels, D., Zhang, H. and Heid, P. (2003). A contextual framework for interpreting the roles of proteins in motility and chemotaxis in *Dictyostelium discoideum. J. Musc. Res. Cell Motil.* **23**, 659-672.

Spudich, J. A. (1989). In pursuit of myosin function. *Cell Regul.* **1**, 1-11.

Stites, J., Wessels, D., Uhl, A., Egelhoff, T. E. Shutt, D. and Soll, D. R. (1998). Phosphorylation of the *Dictyostelium* myosin II heavy chain is necessary for maintaining cellular polarity and suppressing turning during chemotaxis. *Cell Motil. Cytoskeleton* **39**, 31-51.

Varnum, B. and Soll, D. R. (1984). Effect of cAMP on single cell motility in *Dictyostelium*. *J. Cell Biol.* **99**, 1151-1155.

Varnum, B., Edwards, K. B. and Soll, D. R. (1985). *Dictyostelium* amebae

alter motility differently in response to increasing versus decreasing temporal gradients of cAMP. *J. Cell Biol*. **101**, 1-5.

Varnum, B., Edwards, K. and Soll, D. R. (1986). The developmental regulation of single cell motility in *Dictyostelium discoideum*. *Dev. Biol*. **113**, 218-227.

Wessels, D., Soll, D. R., Knecht, D., Loomis, W. F., de Lozanne, A. and Spudich, J. (1988). Cell motility and chemotaxis in *Dictyostelium* amoebae lacking myosin heavy chain. *Dev. Biol*. **128**, 164-177.

Wessels, D., Murray, J. and Soll, D. R. (1992). Behavior of *Dictyostelium* amoebae is regulated primarily by the temporal dynamic of the natural cAMP wave. *Cell Motil. Cytoskeleton* **23**, 145-156.

Wessels, D., Voss, E., von Bergen, N., Burns, R., Stites, J. and Soll, D. R. (1998). A computer-assisted system for reconstructing and interpreting the dynamic three-dimensional relationships of the outer surface, nucleus and pseudopods of crawling cells. *Cell Motil. Cytoskeleton* **41**, 225-246.

Wessels, D. J., Zhang, H., Reynolds, J., Daniels, K., Heid, P., Lu, S., Kuspa, A., Shaulsky, G., Loomis, W. F. and Soll, D. R. (2000). The internal phosphodiesterase RegA is essential for the suppression of lateral pseudopods during *Dictyostelium* chemotaxis. *Mol. Biol. Cell* **11**, 2803-2820.

Wessels, D., Brincks, R., Kuhl, S., Stepanovic, S., Daniels, K. J., Weeks, G., Lim, C. J., Fuller, D., Loomis, W. F. and Soll, D. R. (2004). RasC plays a selective role in the transduction of temporal gradient information in the cAMP wave of *Dictyostelium. Euk. Cell* **3**, 646-662.

Yumura, S. and Uyeda, T. Q. (2003). Myosins and cell dynamics in cellular slime molds. *Int. Rev. Cytol.* **224**, 173-225.

Zhang, H., Wessels, D., Fey, P., Daniels, K., Chisholm, R. and Soll, D. R. (2002). Phosphorylation of the myosin regulatory light chain plays a role in cell motility and polarity during *Dictyostelium* chemotaxis. *J. Cell Sci*. **115**, 1733-1747.

Zhang, H., Heid, P., Wessels, D., Daniels, K., Pham, T., Loomis, W. F. and Soll, D. R. (2003). Constitutively active protein kinase A disrupts motility and chemotaxis in *Dictyostelium discoideum*. *Euk. Cell* **2**, 62-75.

Zigmond, S. H. (1977). The ability of polymorphonuclear leukocytes to orient in gradients of chemotaxis factors. *J. Cell Biol.* **75**, 606-616.